Development of a Plasmonic Biosensor for Bacterial Recognition for Food Safety

Federico Carlesso
Relatore: Ch.mo Prof. Alessandro Paccagnella
Correlatore: Dott. Mauro Perino
Università degli Studi di Padova
Facoltà di Ingegneria
Laurea Magistrale in Ingegneria Elettronica

14 aprile 2014

L' attività di ricerca svolta nella presenti Tesi stata parzialmente
supportata dal progetto intitolato:

*sviluppo di un sensore "label-free" capace di controllare la stabilità
microbiologica dei vini imbottigliati in tempo reale*

finanziato dalla **Regione Veneto** sul bando
**124 - Azione S - COOPERAZIONE PER LO SVILUPPO
DI NUOVI PRODOTTI,
PROCESSI E TECNOLOGIE NEL SETTORE AGRICOLO,
ALIMENTARE E FORESTALE**.

ai miei genitori

Contents

Chapter 1

Introduction

Foodborne diseases represent a serious issue for the public health and for the food industry. In the last 50 years, in order to reduce and to prevent pathogenic contaminations, various techniques for pathogen recognition such as culturing methods have been developed. However, all these techniques require highly specialized laboratory equipment and skilled operators training, making a real time detection difficult.

Conversely, surface plasmon based (SPR) biosensors are portable, simple-to-use sensors which offer the advantage of performing real-time detections, making in-line monitoring of food processing possible.

The main idea behind a SPR sensor is: by modifying the chemical features of a dielectric/metallic interface via molecules with a specific bioaffinity with the target, making it possible to immobilize the desired molecules and recognize them by an optoelectronic instrument.

When developing a SPR sensor, it necessary to achieve specific milestones before reaching the target detection condition. Therefore, the aims of the presented experimental activity are both the optoelectronic characterization of the measurement bench, and the assessment of each sensor surface modification step prior to bacterial detection i.e.

- the metal/air interface condition;
- the functionalized metal surface condition.

This Thesis is organized in three Chapters:

- in Chapter 2 a theoretical review of surface plasmon resonance phenomenon is explained, including the description of the circumstances for the surface plasmon excitation;
- in Chapter 3 a theoretical review of SPR sensors is explained, describing the state of the art for SPR sensors in the food safety field. A simulation software and the measurement bench used are described as well.

- in Chapter 4 the experimental results are shown: these include bench characterization tests, bare devices tests, functionalized metal tests and an antibodies immobilization test.

As will be described in the final Chapter, the optoelectronic system is able to discern each different functionalization step from the bare sensor, with a sensitivity similar to that reported in literature for comparable measurement systems.

Chapter 2

Electromagnetics of metals

Plasmonics forms a major part of the field of *nanophotonics*, which describes how electromagnetic fields can be confined into a material whose dimensions are on the order or smaller than the wavelength. It is based on the interaction process between electromagnetic radiation and conduction electrons at metallic/dielettric interfaces. This interaction consists in surface waves whose mathematical description was established around the beginning of 20^{th} century. They were described in the context of radio waves propagating along the surface of a conductor of finite conductivity. In the visible range, the observation of "intensity drops" in spectra produced when visible light reflects at metallic gratings [1] was not connected with the earlier theoretical work until 1941 [2]. However, only in 1968 the excitation of Sommerfeld's surface waves with visible light using prism coupling was achieved. Hence, in those years a unified descriptions of these phenomena in the form of surface plasmon polaritons was established.

2.1 Maxwell's Equations

The first description of "surface plasmon waves" was based on a classical framework derived by Maxwell's equations. It remains a valid starting point for a mathematical description of the polaritons, avoiding the need to resort to quantum mechanics. However, this description does not prevent a rich and often unexpected variety of optical phenomena, which need a more complicated description to be correctely understood. The macroscopic electromagnetism Maxwell's equations can be expressed as [3]:

$$\nabla \cdot \mathbf{d} = \rho_{ext} \tag{2.1}$$

$$\nabla \cdot \mathbf{b} = 0 \tag{2.2}$$

$$\nabla \times \mathbf{e} = -\frac{\partial \mathbf{b}}{\partial t} \tag{2.3}$$

$$\nabla \times \mathbf{h} = \mathbf{j}_{ext} + \frac{\partial \mathbf{d}}{\partial t} \tag{2.4}$$

These equations create a link between the four macroscopic fields **d** (dielectric displacement), **e** (the electric field), **h** (the magnetic field) and **b** (the magnetic flux density) and external charge and current densities. These four fields are further linked via the polarization **p** and magnetization **m**

$$\mathbf{d} = \epsilon_0 \mathbf{e} + \mathbf{p} \tag{2.5}$$

$$\mathbf{h} = \frac{1}{\mu_0}\mathbf{b} - \mathbf{m} \tag{2.6}$$

where ϵ_0 and μ_0 are the electric permettivity and magnetic permeability of vacuum. Considering nonmagnetic media, $\mathbf{m} = 0$ while **p** describes the electic dipole moment per unite volume inside the material, caused by the alignement of microscopic dipoles with the electric field. Remembering that $\nabla \cdot \mathbf{p} = \rho$ and that for charge conservation $\nabla \cdot \mathbf{j} = -\frac{\partial \rho}{\partial t}$, it is possible to write

$$\mathbf{j} = \frac{\partial \mathbf{p}}{\partial t} \tag{2.7}$$

Hence, rearranging previous equations

$$\nabla \cdot \mathbf{e} = \frac{\rho_{tot}}{\epsilon_0} \tag{2.8}$$

In a general description, **d** and **e**, **b** and **h** are linked by the following relations:

$$\mathbf{d}(\mathbf{r}, t) = \int\int \mathbf{G}(\mathbf{r}, t, \mathbf{r'}, t')\mathbf{e}(\mathbf{r'}, t')d\mathbf{r'}dt' \tag{2.9}$$

$$\mathbf{b}(\mathbf{r}, t) = \int\int \mathbf{M}(\mathbf{r}, t, \mathbf{r'}, t')\mathbf{h}(\mathbf{r'}, t')d\mathbf{r'}dt' \tag{2.10}$$

where **G** and **M** are 3x3 matrices which can be simplified in case of a medium with the following characteristics:

- linear;
- isotropic;
- nondispersive in time and space;

obtaining

$$\mathbf{d}(\mathbf{r}, t) = G(\mathbf{r}, t)\mathbf{e} = \epsilon(\mathbf{r}, t)\mathbf{e}(\mathbf{r}, t) \tag{2.11}$$

$$\mathbf{b}(\mathbf{r}, t) = M(\mathbf{r}, t)\mathbf{h}(\mathbf{r}, t) = \mu(\mathbf{r}, t)\mathbf{h}(\mathbf{r}, t) \tag{2.12}$$

which, in case of homogeneity in time and space, yield to

$$\mathbf{d}(\mathbf{r}, t) = \epsilon_0 \epsilon_r \mathbf{e}(\mathbf{r}, t) \tag{2.13}$$

$$\mathbf{b}(\mathbf{r},t) = \mu_0\mu_r\mathbf{h}(\mathbf{r},t) \tag{2.14}$$

where ϵ_r is the relative permettivity in the medium and $\mu_r = 1$ is the relative permeability of the nonmagnetic medium. The linear relationship between **d** and **e** is often defined using the dielectric supsceptibility χ, so that $\mathbf{p} = \epsilon_0\chi\mathbf{e}$, yielding $\epsilon_r = 1 + \chi$.
The last important relation is:

$$\mathbf{j}(\mathbf{r},t) = \int\int \mathbf{F}(\mathbf{r},t,\mathbf{r'},t')\mathbf{e}(\mathbf{r'},t')d\mathbf{r'}dt' \tag{2.15}$$

which, in case of isotropic, linear and nondispersive medium, can be reduced to

$$\mathbf{j}(\mathbf{r},t) = \gamma(\mathbf{r},t)\mathbf{e}(\mathbf{r},t) \tag{2.16}$$

which comes out from the conduction theory of carriers into metallic materials (Ohm's law).

2.1.1 In the Time Domain

It is not easy the calculation of Maxwell's equations when the medium is not insulator: when $\gamma = 0$ Maxwell's equations are esily found out, obtaining the well-famous **D'Alambert equation**

$$\nabla^2\mathbf{h} - \mu\epsilon\frac{\partial^2\mathbf{h}}{\partial t^2} = 0 \tag{2.17}$$

which is solved by equations in the form of

$$\mathbf{h}(\mathbf{r},t) = f(\mathbf{r} - \mathbf{v}t) + g(\mathbf{r} + \mathbf{v}t) \tag{2.18}$$

When the medium is not insulator ($\gamma \neq 0$) the D'Alambert equation is in the form

$$\nabla^2\mathbf{h} - \mu\epsilon\frac{\partial^2\mathbf{h}}{\partial t^2} - \gamma\mu\frac{\partial\mathbf{h}}{\partial t} = 0 \tag{2.19}$$

To simplify the derivation of the solutions, the Maxwell's equations are transferred to frequency domain by applying Fourier/Helmholtz transform.

2.1.2 In the Frequency Domain

From equation (2.9) and (2.15) it's possible to obtain the so-called **dieletric function** by applying the Fourier Transform [4]:

$$\mathbf{D}(\mathbf{K},\omega) = \epsilon_0\epsilon_r(\mathbf{K},\omega)\mathbf{E}(\mathbf{K},\omega) \tag{2.20}$$

$$\mathbf{J}(\mathbf{K},\omega) = \gamma(\mathbf{K},\omega)\mathbf{E}(\mathbf{K},\omega) \tag{2.21}$$

where $\mathbf{K}$ is the wavevector.
By appling $\mathbf{D} = \epsilon_0\mathbf{E} + \mathbf{P}$ and $\mathbf{J} = j\omega\mathbf{P}$, remembering that the derivative in the Fourier domain results in $j\omega$, it's possible to obtain

$$\epsilon_r(\mathbf{K}, \omega) = 1 + \frac{j\gamma(\mathbf{K}, \omega)}{\epsilon_0\omega} \tag{2.22}$$

which can be simplified in interaction of light with metals to $\epsilon_r(\mathbf{K{=}0}, \omega) = \epsilon_r(\omega)$. Hence, the dielectric function depends on frequency and could be represented as a complex number

$$\epsilon(\omega) = \epsilon_1(\omega) + j\epsilon_2(\omega)$$

and

$$\gamma(\omega) = \gamma_1(\omega) + j\gamma_2(\omega)$$

Those values yield the determination of the complex refractive index [5]

$$\tilde{n}(\omega) = n(\omega) + j\kappa(\omega)$$

, where $\tilde{n}(\omega) = \sqrt{\epsilon_r(\omega)}$

Some books (for example [3] or [5]) define the complex quantity

$$\epsilon_c = \epsilon - \frac{j\gamma}{\omega} \tag{2.23}$$

as a complex dieletric permittivity, a quantity which can be useful to simplify the Maxwell's equations in Steinmetz representation.
It should be noticed that the difference in representation ((2.22) and (2.23)) is mainly due to the dimensions: in electromagnetic fields theory for small materials (nanometers thickness) like polaritons the (2.22) is mostly used.

Another quantity, called *loss angle* is defined as

$$\delta = \arctan\left(\frac{\gamma}{\omega\epsilon}\right) \tag{2.24}$$

which is an angle whose range is $0 \leq \delta \leq \frac{\pi}{2}$. It is a value that gives quantitative information about the conductibility of the material. A good conductor is defined when $\frac{\gamma}{\omega\epsilon} \gg 1$.

Hence, applying the Steinmetz transformation, supposing that vectors could be written as exponential functions

$$\mathbf{e}(\mathbf{r}, t) = \mathbf{E}(\mathbf{r})e^{j\omega t} \rightarrow \mathbf{E}(\mathbf{r})$$

$$\mathbf{h}(\mathbf{r}, t) = \mathbf{H}(\mathbf{r})e^{j\omega t} \rightarrow \mathbf{H}(\mathbf{r})$$

$$\mathbf{b}(\mathbf{r}, t) = \mathbf{B}(\mathbf{r})e^{j\omega t} \rightarrow \mathbf{B}(\mathbf{r})$$

$$\mathbf{d}(\mathbf{r}, t) = \mathbf{D}(\mathbf{r})e^{j\omega t} \rightarrow \mathbf{D}(\mathbf{r})$$

$$\mathbf{j}(\mathbf{r},t)=\mathbf{J}(\mathbf{r})e^{j\omega t}\rightarrow\mathbf{J}(\mathbf{r})$$

it is possible to derive Maxwell's equations in the frequency domain

$$\begin{cases}\nabla\times\mathbf{E}=-j\omega\mathbf{B}=-j\omega\mu\mathbf{H}\\ \nabla\times\mathbf{H}=j\omega\epsilon_c\mathbf{E}\end{cases}\tag{2.25}$$

Now, applying the operator $\nabla\times$ at the left and right side of the first equation

$$\nabla\times\nabla\times\mathbf{E}=-j\omega\mu(\nabla\times\mathbf{H})=\omega^2\mu\epsilon_c\mathbf{E}$$

and, recalling the simple relation $\nabla\times\nabla\times\mathbf{E}=-\nabla^2\mathbf{E}+\nabla(\nabla\cdot\mathbf{E})$, in case of absence of external stimuli $\rho=0\rightarrow\nabla\cdot\mathbf{E}=0$ and in case of homogeneity of the medium (ϵ_c =constant), the **Helmholtz equation** is obtained:

$$\nabla^2\mathbf{E}+\omega^2\mu\epsilon_c\mathbf{E}=0\tag{2.26}$$

It can be also rewritten in the following form

$$\nabla^2\mathbf{E}-\sigma^2\mathbf{E}=0\qquad\qquad\sigma^2=-\omega^2\mu\epsilon_c\tag{2.27}$$

or in the form

$$\nabla^2\mathbf{E}+k_0^2\epsilon_r\mathbf{E}=0\qquad\qquad k_0=\frac{\omega}{c}\tag{2.28}$$

To solve it, it can be assumed that the solution can be written in the form $\mathbf{E}(x,y,z)=\mathbf{E}(z)e^{j\beta x}$, where $\beta=k_x$ is called propagation constant in the x-direction, leading to

$$\nabla^2\mathbf{E}(x,y,z)=\frac{\partial^2\mathbf{E}(x,y,z)}{\partial x^2}+\frac{\partial^2\mathbf{E}(x,y,z)}{\partial y^2}+\frac{\partial^2\mathbf{E}(x,y,z)}{\partial z^2}=$$
$$=e^{j\beta x}\left(\frac{\partial^2\mathbf{E}(z)}{\partial z^2}-\beta^2\mathbf{E}(z)\right)$$

Hence, it's possibile to rewrite the **Helmholz equations** in the form:

$$\frac{\partial^2\mathbf{E}}{\partial z^2}+\left(k_0^2\epsilon_r-\beta^2\right)\mathbf{E}=0\tag{2.29}$$

A similar equation can be found for **H**. However, in case of reducing **H**, there is the need of $\mathbf{J}=0$ (absence of external stimuli).
From equations

$$\begin{cases}\nabla\times\mathbf{E}=-j\omega\mathbf{B}=-j\omega\mu_0\mathbf{H}\\ \nabla\times\mathbf{H}=j\omega\epsilon_0\epsilon_r\mathbf{E}\end{cases}$$

it's possible to obtain the following relations:

$$\begin{pmatrix}\frac{\partial E_z}{\partial y}-\frac{\partial E_y}{\partial z}\\ \frac{\partial E_x}{\partial z}-\frac{\partial E_z}{\partial x}\\ \frac{\partial E_y}{\partial x}-\frac{\partial E_x}{\partial y}\end{pmatrix}=j\omega\mu_0\begin{pmatrix}H_x\\ H_y\\ H_z\end{pmatrix}$$

$$\begin{pmatrix} \frac{\partial H_z}{\partial y} - \frac{\partial H_y}{\partial z} \\ \frac{\partial H_x}{\partial z} - \frac{\partial H_z}{\partial x} \\ \frac{\partial H_y}{\partial x} - \frac{\partial H_x}{\partial y} \end{pmatrix} = -j\omega\epsilon_0\epsilon_r \begin{pmatrix} E_x \\ E_y \\ E_z \end{pmatrix}$$

and, for solutions in the form $\mathbf{E}(x,y,z) = \mathbf{E}(z)e^{j\beta x}$, and $\mathbf{H}(x,y,z) = \mathbf{H}(z)e^{j\beta x}$, the previous equations are reduced to

$$\begin{pmatrix} \frac{\partial E_y}{\partial z} \\ \frac{\partial E_x}{\partial z} - j\beta E_z \\ j\beta E_y \end{pmatrix} = j\omega\mu_0 \begin{pmatrix} -H_x \\ H_y \\ H_z \end{pmatrix}$$

$$\begin{pmatrix} \frac{\partial H_y}{\partial z} \\ \frac{\partial H_x}{\partial z} - j\beta H_z \\ j\beta H_y \end{pmatrix} = -j\omega\epsilon_0\epsilon_r \begin{pmatrix} -E_x \\ E_y \\ E_z \end{pmatrix}$$

These equations lead to two sets of solutions:

- **TM** or **p modes**, in which the magnetic field is orthogonal to the propagation direction $H_x = 0$. Sobstituting $H_x = 0$ in the previous relations, $H_z = 0$ and $E_y = 0$ are obtained

  $$\begin{pmatrix} E_x \\ E_y \\ E_z \end{pmatrix} = \begin{pmatrix} -j\frac{1}{\omega\epsilon_0\epsilon_r}\frac{\partial H_y}{\partial z} \\ 0 \\ -\frac{\beta}{\omega\epsilon_0\epsilon_r}H_y \end{pmatrix} \tag{2.30}$$

  and the wave equation is:

  $$\frac{\partial^2 H_y}{\partial z^2} + (k_0^2\epsilon_r - \beta^2)H_y = 0 \tag{2.31}$$

- **TE** or **s modes**, in which the electric field is orthogonal to the propagation direction $E_x = 0$. Sobstituting $E_x = 0$ in the previous relations, $E_z = 0$ and $H_y = 0$ are obtained

  $$\begin{pmatrix} H_x \\ H_y \\ H_z \end{pmatrix} = \begin{pmatrix} j\frac{1}{\omega\mu_0}\frac{\partial E_y}{\partial z} \\ 0 \\ -\frac{\beta}{\omega\mu_0}E_y \end{pmatrix} \tag{2.32}$$

  and the wave equation is:

  $$\frac{\partial^2 E_y}{\partial z^2} + (k_0^2\epsilon_r - \beta^2)E_y = 0 \tag{2.33}$$

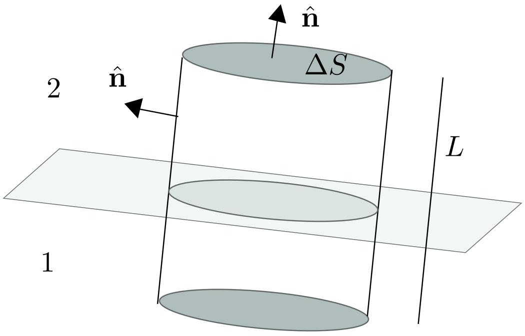

Figure 2.1: Gauss cylinder

2.2 Continuity Relations

Continuity relations are fundamental relations used to describe the behaviour of Electric and Magnetic fields at an interface between two media. In this section two media as in Figure 2.1 are considered.

- **Continuity for Dielectric Displacement**

  Considering the Figure 2.1, it is possible to use the **Gauss Theorem**, leading to

  $$\oint \mathbf{d} \cdot \hat{\mathbf{n}} \ dS = q$$

  where $\hat{\mathbf{n}}$ is the Unit Vector orthogonal to the surface in each point. Solving,

  $$-\Delta S \mathbf{d}_1 \cdot \hat{\mathbf{n}} + \Delta S \mathbf{d}_2 \cdot \hat{\mathbf{n}} + \Phi_2 = q$$

  where Φ_2 is the lateral flux, and

  $$-\Delta S \mathbf{d}_1 \cdot \hat{\mathbf{n}} + \Delta S \mathbf{d}_2 \cdot \hat{\mathbf{n}} = \Delta Q_s \qquad \Phi_2 = 0 \qquad L \to 0$$

  $$\Delta S (\mathbf{d}_2 - \mathbf{d}_1) \cdot \hat{\mathbf{n}} = \lim_{L \to 0} q = \Delta Q_s$$

  where ΔQ_s is the surface charge.

  $$(\mathbf{d}_2 - \mathbf{d}_1) \cdot \hat{\mathbf{n}} = \lim_{\Delta S \to 0} \frac{\Delta Q_s}{\Delta S} = \rho_s$$

  When the surface density charge is zero, $\rho_s = 0$,

  $$\mathbf{d}_1 \cdot \hat{\mathbf{n}} = \mathbf{d}_2 \cdot \hat{\mathbf{n}} \ \Rightarrow \ \mathbf{d}_{n_1} = \mathbf{d}_{n_2} \tag{2.34}$$

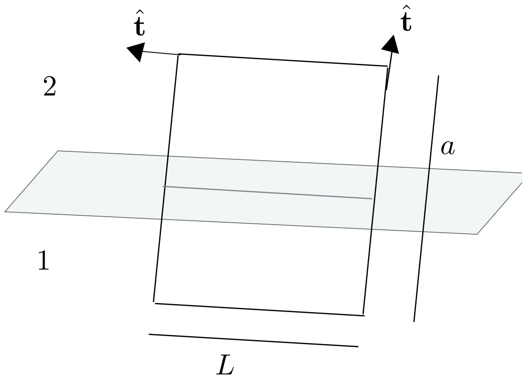

Figure 2.2: Coil

- **Continuity for Flux Density Field**
  Considering Figure 2.1, it is possible to obtain
  $$\oint \mathbf{b} \cdot \hat{\mathbf{n}} \; dS = 0$$
  from which, repeating the process for dielectric displacement,
  $$\mathbf{b}_1 \cdot \hat{\mathbf{n}} = \mathbf{b}_2 \cdot \hat{\mathbf{n}} \;\; \Rightarrow \;\; \mathbf{b}_{n_1} = \mathbf{b}_{n_2} \tag{2.35}$$

- **Continuity for Magnetic Field**
  In this case a coil is considered instead of the cylindric volume. $\hat{\mathbf{t}}$ is the tangent Unit Vector to the plane interface.
  $$\oint_c \mathbf{h} \cdot \hat{\mathbf{c}} \; dc = \int_{Surf_c} \frac{\partial \mathbf{d}}{\partial t} \cdot \hat{\mathbf{n}} \; dS + \int_{Surf_c} \mathbf{J} \cdot \hat{\mathbf{n}} \; dS$$
  $$L(\mathbf{h}_2 - \mathbf{h}_1)\hat{\mathbf{t}} + C = \frac{\partial \Phi_d}{\partial t} + I$$
  where C is the contribution of the vertical part of the coil, Φ_d is the flux through the coil and I is the current which passes in the coil. When $a \to 0$, $C \to 0$ and $\Phi_d \to 0$ because the surface area goes to zero. Hence, the equation is reduced to
  $$L(\mathbf{h}_2 - \mathbf{h}_1)\hat{\mathbf{t}} = \Delta I_s$$
  and, when $L \to 0$
  $$(\mathbf{h}_2 - \mathbf{h}_1) \cdot \hat{\mathbf{t}} = \lim_{L \to 0} \frac{\Delta I_s}{L} = J_s$$

When $J_s = 0$

$$\mathbf{h}_2 \cdot \hat{\mathbf{t}} = \mathbf{h}_1 \cdot \hat{\mathbf{t}} \;\; \Rightarrow \;\; \mathbf{h}_{t_1} = \mathbf{h}_{t_2} \tag{2.36}$$

- **Continuity for Electric Field**
  Considering Figure 2.2, an analogous analysis to magnetic field could be performed for electric field, finding

$$\mathbf{e}_{t_1} = \mathbf{e}_{t_2} \tag{2.37}$$

2.3 Surface Plasmon Polaritons at a Single Interface

Consider a single flat interface between a dielectric, non absorbing half space with positive real relative permittivity ϵ_{r_2} and a conducting half space with $\epsilon_{r_1}(\omega)$ as a dielectric function [4], as represented in Figure 2.3.

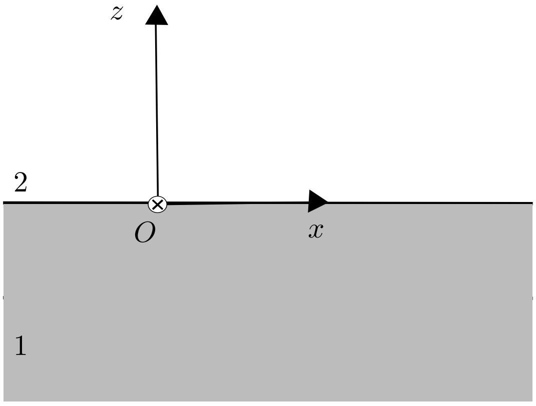

Figure 2.3: Coordinate system between two semi-infinite media

It is possible to analyze distinctely the two cases:

- In **TM modes**, solutions of $\frac{\partial^2 H_y}{\partial z^2} + (k_0^2\epsilon_r - \beta^2)H_y = 0$ can be written in the form

$$H_y = H_y(z)e^{j\beta x} = Ae^{\pm\sqrt{\beta - k_0^2\epsilon_r}z}e^{j\beta x} = Ae^{\pm k_z z}e^{j\beta x}$$

  where ± depends on the position in the coordinate system.

  In the second medium, assuming $z > 0$, the magnetic field can be written as

$$\begin{pmatrix} H_x \\ H_y \\ H_z \end{pmatrix} = \begin{pmatrix} 0 \\ A_2 e^{-k_{z_2} z} e^{j\beta x} \\ 0 \end{pmatrix} \tag{2.38}$$

and the electric field as

$$\begin{pmatrix} E_x \\ E_y \\ E_z \end{pmatrix} = \begin{pmatrix} jA_2 \frac{1}{\omega \epsilon_0 \epsilon_{r_2}} k_{z_2} e^{-k_{z_2} z} e^{j\beta x} \\ 0 \\ -A_2 \frac{\beta}{\omega \epsilon_0 \epsilon_2} e^{j\beta x} e^{-k_{z_2} z} \end{pmatrix} \tag{2.39}$$

In the first medium, assuming $z < 0$, the magnetic field can be written as

$$\begin{pmatrix} H_x \\ H_y \\ H_z \end{pmatrix} = \begin{pmatrix} 0 \\ A_1 e^{k_{z_1} z} e^{j\beta x} \\ 0 \end{pmatrix} \tag{2.40}$$

and the electric field as

$$\begin{pmatrix} E_x \\ E_y \\ E_z \end{pmatrix} = \begin{pmatrix} -jA_1 \frac{1}{\omega \epsilon_0 \epsilon_{r_1}} k_{z_1} e^{k_{z_1} z} e^{j\beta x} \\ 0 \\ -A_1 \frac{\beta}{\omega \epsilon_0 \epsilon_1} e^{j\beta x} e^{k_{z_1} z} \end{pmatrix} \tag{2.41}$$

k_z is the component of the wave vector orthogonal to the interface (found at $z = 0$) while β is the component of the wave vector parallell to the interface. Now, it is possible to apply the Continuity Conditions found in Section 2.2.

$$H_{y_2}(z = 0) = H_{y_1}(z = 0) \;\; \Rightarrow \;\; A_1 = A_2$$

$$\epsilon_2 E_{z_2}(z = 0) = \epsilon_1 E_{z_1}(z = 0) \;\; \Rightarrow \;\; A_1 = A_2$$

$$E_{x_2}(z = 0) = E_{x_1}(z = 0) \;\; \Rightarrow \;\; \frac{k_{z_2}}{\epsilon_{r_2}} = -\frac{k_{z_1}}{\epsilon_{r_1}}$$

Because of the choice of $Re\left[k_{z_1}\right] > 0$ and $Re\left[k_{z_2}\right] > 0$, necessarily $Re\left[\epsilon_{r_1}\right] > 0$ and $Re\left[\epsilon_{r_2}\right] < 0$ or vice versa. Hence mathematically one of the media needs to be a metal (metals have relative permittivity whose real part is negative) and the other an insulator: we can choose medium 1 as the metal and medium 2 as the insulator, according to the physical choice of the beginning of the section.
k_{z_2} and k_{z_1} need to fulfill the wave equation, leading to

$$k_{z_1}^2 = \beta^2 - k_0^2 \epsilon_{r_1} \tag{2.42}$$

$$k_{z_2}^2 = \beta^2 - k_0^2 \epsilon_{r_2} \tag{2.43}$$

Combining these last three equations the following relation is obtained [6]:

$$\beta = k_0 \sqrt{\frac{\epsilon_{r_1} \epsilon_{r_2}}{\epsilon_{r_1} + \epsilon_{r_2}}} = k_{SPP} \tag{2.44}$$

This expression is valid for both real and complex part: it is the *Dispersion relation* of SPPs propagating at the interface between two half spaces. Because β is complex, it can be rewritten in the form

$$\beta = \beta_1 + j\beta_2$$

and, considering $\epsilon_{r_1} = \epsilon_{r_{1_1}} + j\epsilon_{r_{1_2}}$ and ϵ_{r_2} as dielectric function and constant for metallic and dielectric medium respectively, it's possible to obtain

$$\beta = k_0\sqrt{\frac{\epsilon_{r_{1_1}}\epsilon_{r_2} + j\epsilon_{r_{2_1}}\epsilon_{r_2}}{\epsilon_{r_{1_1}} + \epsilon_{r_2} + j\epsilon_{r_{2_1}}}} \tag{2.45}$$

When $|\epsilon_{r_{1_1}}| \gg \epsilon_{r_{1_2}}$, the complex propagation constant of the surface plasmon could be expressed as

$$\beta = \beta_1 + j\beta_2 = k_0\sqrt{\frac{\epsilon_{r_{1_1}}\epsilon_{r_2}}{\epsilon_{r_{1_1}} + \epsilon_{r_2}}} + j\frac{\epsilon_{r_{1_2}}}{2\epsilon_{r_{1_1}}^2}k_0\left(\frac{\epsilon_{r_{1_1}}\epsilon_{r_2}}{\epsilon_{r_{1_1}} + \epsilon_{r_2}}\right)^{\frac{3}{2}} \tag{2.46}$$

As follows from this equation, the imaginary part of the permittivity of metal $\epsilon_{r_{1_2}}$ causes the propagation constant of a surface plasmon to have a non-zero imaginary part, which is associated with attenuation of the surface plasmon. The attenuation is sometimes characterized by the propagation length L, which is defined as the distance in the direction of propagation at which the energy of the surface plasmon decreases by a factor of e^{-1}:

$$L = \frac{1}{2\beta_2} \tag{2.47}$$

As follows from previous equations of the electric and magnetic field in both media, the field amplitude of the SPs decreases exponentially as $e^{-|k_{z_1}||z|}$ in the medium 1 and as $e^{-|k_{z_2}||z|}$ in the medium 2 in the direction normal to the interface. The value of the (skin) depth at which the field falls to e^{-1} becomes

$$\hat{z}_1 = \frac{1}{|k_{z_1}|} \qquad \hat{z}_2 = \frac{1}{|k_{z_2}|} \tag{2.48}$$

and so, sobstituting k_z for each medium, it is possible to get:

$$\hat{z}_1 = \frac{1}{k_0}\sqrt{\frac{\epsilon_{r_{1_1}} + \epsilon_{r_2}}{\epsilon_{r_{1_1}}^2}} \qquad \hat{z}_2 = \frac{1}{k_0}\sqrt{\frac{\epsilon_{r_{1_1}} + \epsilon_{r_2}}{\epsilon_{r_2}^2}} \tag{2.49}$$

- In **TE modes**, solutions of $\frac{\partial^2 E_y}{\partial z^2} + (k_0^2\epsilon_r - \beta^2)E_y = 0$ can be written in the form

$$E_y = E_y(z)e^{j\beta x} = Ae^{\pm\sqrt{\beta - k_0^2\epsilon_r}z}e^{j\beta x} = Ae^{k_z z}e^{j\beta x}$$

where ± depends on the position in the coordinate system.

In the second medium, assuming $z > 0$, the magnetic field can be written as

$$\begin{pmatrix} H_x \\ H_y \\ H_z \end{pmatrix} = \begin{pmatrix} -jA_2 \frac{1}{\omega\mu_0} k_{z_2} e^{j\beta x} e^{-k_{z_2} z} \\ 0 \\ A_2 \frac{\beta}{\omega\mu_0} e^{j\beta x} e^{-k_{z_2} z} \end{pmatrix} \tag{2.50}$$

and the electric field

$$\begin{pmatrix} E_x \\ E_y \\ E_z \end{pmatrix} = \begin{pmatrix} 0 \\ A_2 e^{j\beta x} e^{-k_{z_2} z} \\ 0 \end{pmatrix} \tag{2.51}$$

In the first medium, assuming $z < 0$, the magnetic field can be written as

$$\begin{pmatrix} H_x \\ H_y \\ H_z \end{pmatrix} = \begin{pmatrix} jA_1 \frac{1}{\omega\mu_0} k_{z_1} e^{j\beta x} e^{k_{z_1} z} \\ 0 \\ A_1 \frac{\beta}{\omega\mu_0} e^{j\beta x} e^{k_{z_1} z} \end{pmatrix} \tag{2.52}$$

and the electric field

$$\begin{pmatrix} E_x \\ E_y \\ E_z \end{pmatrix} = \begin{pmatrix} 0 \\ A_1 e^{j\beta x} e^{k_{z_1} z} \\ 0 \end{pmatrix} \tag{2.53}$$

Now, it is possible to apply the Continuity Conditions found in Section 2.2

$$H_{z_1}(z=0) = H_{z_2}(z=0) \quad \Rightarrow \quad A_1 = A_2$$

$$E_{y_1}(z=0) = E_{y_2}(z=0) \quad \Rightarrow \quad A_1 = A_2$$

$$H_{x_1}(z=0) = H_{x=2}(z=0) \quad \Rightarrow \quad -k_{z_1} = -k_{z_2}$$

Since confinement to the surface requires $Re\left[k_{z_1}\right] > 0$ and $Re\left[k_{z_2}\right] > 0$, these conditions can be satisfied only when $A_1 = A_2 = 0$. Hence, there aren't any modes for TE polarization.

2.4 Lorenz-Drude Model

The Lorenz-Drude equation [4] provides a simple model of material's relative permittivity that works quite well in practice. While the derivation is general (it can be extended to crystaline solids), the model is usually used with metals. In this model the electron is bound to the atom's nucleus and it is free to oscillate like a mass on a spring. In absence of applied field it can be described by:

$$m\ddot{\mathbf{r}} + m\gamma\dot{\mathbf{r}} + C\mathbf{r} = 0 \tag{2.54}$$

where $\mathbf{r}$ is the electron position (the nucleus is considered as the origin), C is the spring constant, m is the electron mass and γ is the damping factor. The resonance frequency can be defined as

$$\omega_0 = \sqrt{\frac{C}{m}} \tag{2.55}$$

When applied a time-harmonic field, in the form of $E_0 e^{j\omega t}$, the equation becomes

$$\ddot{\mathbf{r}} + \gamma\dot{\mathbf{r}} + \omega_0^2 \mathbf{r} = -\frac{e}{m}\mathbf{E}_0 e^{j\omega t} \tag{2.56}$$

where e is the electron charge. Assuming $\mathbf{r} = \mathbf{r}_0 e^{j\omega t}$ the equation becomes

$$(-\omega^2 + j\omega\gamma + \omega_0^2)\mathbf{r}_0 = -\frac{e}{m}\mathbf{E}_0$$

The dipole momentum of one electron is given by $\mathbf{p} = -e\mathbf{r}$, so

$$\mathbf{p}_0 = \frac{e^2}{m(\omega_0^2 - \omega^2 + j\omega\gamma)}\mathbf{E}_0 \tag{2.57}$$

In a region with atomic density N, considering $\mathbf{E}_0$ constant and the interaction between adjacent atoms neglegible, the total polarization is given by:

$$\mathbf{P} = \frac{Ne^2}{m(\omega_0^2 - \omega^2 + j\omega\gamma)}\mathbf{E}_0 \tag{2.58}$$

Thus, from the constitutive relation $\mathbf{D} = \epsilon_0\mathbf{E} + \mathbf{P} = \epsilon_r\epsilon_0\mathbf{E}$

$$\epsilon(\omega) = 1 + \frac{\omega_p^2}{\omega_0^2 - \omega^2 + j\omega\gamma} \tag{2.59}$$

where the plasma frequency ω_p has been introduced, defined as

$$\omega_p = \frac{Ne^2}{\epsilon_0 m} \tag{2.60}$$

In case of a metal, the dielectric function is approximated by a free electron gas. In this case, there isn't any restoring forces on the free conduction electrons. For this reason $\omega_0 = 0$ simplifying the previous equation in

$$\epsilon_r(\omega) = 1 - \frac{\omega_p^2}{\omega^2 - j\omega\gamma} \tag{2.61}$$

In this context, the damping factor can be considered as the collision frequency (the inverse of the time between collisions of a conduction electron). For typical metals, $\gamma = \frac{1}{\tau} = 10^{-14}s^{-1}$

The real and imaginary components of this complex dielectric function $\epsilon_r(\omega) = \epsilon_{r_1}(\omega) + j\epsilon_{r_2}(\omega)$ are given by:

$$\epsilon_{r_1}(\omega) = 1 - \frac{\omega_p^2\tau^2}{1+\omega^2\tau^2} \tag{2.62}$$

$$\epsilon_{r_2}(\omega) = \frac{\omega_p^2\tau}{\omega(1+\omega^2\tau^2)} \tag{2.63}$$

Considering only frequencies $\omega < \omega_p$, metals retain their metallic character and they are mainly absorbing.
For higher frequencies ($1 \leq \omega\tau \leq \omega_p\tau$) the complex refractive index is predominantly imaginary (leading to a reflection coefficient $R \approx 1$) [7], and σ acquires more and more complex character.
For frequencies close to ω_p the product $\omega\tau \gg 1$ leads to a *Neglegible Damping Model* (it refers to a model in which there is absence of damping in $\epsilon(\omega)$ when ω grows from $\omega_p - \delta$ to $\omega_p + \delta$). In this model, when ω is close to ω_p, $\epsilon(\omega)$ is predominantly real and

$$\epsilon_r(\omega) = 1 - \frac{\omega_p^2}{\omega^2} \tag{2.64}$$

can be taken as the dielectric funcion of the undamped free electron plasma.

However, until this point the description has assumed an ideal free-electron model. Real metals have a certain number of resonances and hence an extension of this model is needed. For this reason, their permittivity could be expressed better as a sum of Lorentz-Drude terms, each with different ω_p and γ. However, when looking at a limited frequency range, it is usually more convenient to lump all of the higher-frequency resonances together, and represent their contribution by the term ϵ_∞ which would replace the 1 in Equation (2.61).
Sometimes it is more convenient to work in terms of wavelengths rather than frequency. Hence, the Lorenz-Drude equation becomes

$$\epsilon_r(\lambda) = 1 - \frac{\omega_p^2\lambda^2}{(2\pi c)^2 - j2\pi c\gamma\lambda} \tag{2.65}$$

where c is the speed of light.

2.5 Calculation of Relative Permittivity

All materials have a wavelength-dependent dielectric “constant”. It is possible to use tables to find measured values; however, when a limited wavelength band is considered, the relative permittivity can be well approximated by a simple equation. For this reason it’s possible to consider two different empirical formulas [8], valid for transparent medium:

- $$n(\lambda) = A + \frac{B}{\lambda^2} + \frac{C}{\lambda^4} \tag{2.66}$$

  which is well-known as *Cauchy Equation*. It works correctly in the visible wavelength region;

- $$n(\lambda)^2 = \epsilon(\lambda) = 1 + \frac{B_1\lambda^2}{\lambda^2 - C_1} + \frac{B_2\lambda^2}{\lambda^2 - c_2} + \frac{B_3\lambda^2}{\lambda^2 - C_3} \tag{2.67}$$

  which is the *Sellmeier Equation*.

Both of them depend on parameters (capital letters) which are obtained from data and scaled to work with convenient units. However, there is no apparently industry standard, and coefficients given on different manufacture's data sheets are likely to use different scaling.

2.6 Analysis of Dispersion Relation

In previous sections the dispersion relation has been obtained. From (2.44):

$$k_{SPP} = \beta = k_0\sqrt{\frac{\epsilon_{r_1}\epsilon_{r_2}}{\epsilon_{r_1} + \epsilon_{r_2}}}$$

and, considering ω close to ω_p, from (2.64), assuming ϵ_{r_1} real,

$$\epsilon_{r_1}(\omega) = 1 - \frac{\omega_p^2}{\omega^2}$$

Therefore, it is possible to obtain

$$\frac{\beta c}{\omega_p} = \frac{\omega}{\omega_p}\sqrt{\frac{\epsilon_{r_2}(1 - \frac{\omega_p^2}{\omega^2})}{1 + \epsilon_{r_2} - \frac{\omega_p^2}{\omega^2}}} \tag{2.68}$$

This equation is plotted in Figure 2.4 for two different media (*air* $\epsilon_{r_2} = 1$ and *fused silica* $\epsilon_{r_2} = 2.25$), representing the wavevector $\beta c/\omega_p$ as a function of frequency normalized to the plasma frequency ω_p. Both real (continuous curves) and imaginary parts (dotted curves) of β are shown. The *light lines* in air and fused silica are shown, as well. They are obtained by

$$k = \frac{2\pi}{\lambda} = \frac{\omega n}{c}$$

leading to

$$\frac{kc}{\omega_p} = \frac{\omega\sqrt{\epsilon_{r_2}}}{\omega_p} \tag{2.69}$$

It is the wavevector of the light travelling in a certain medium.

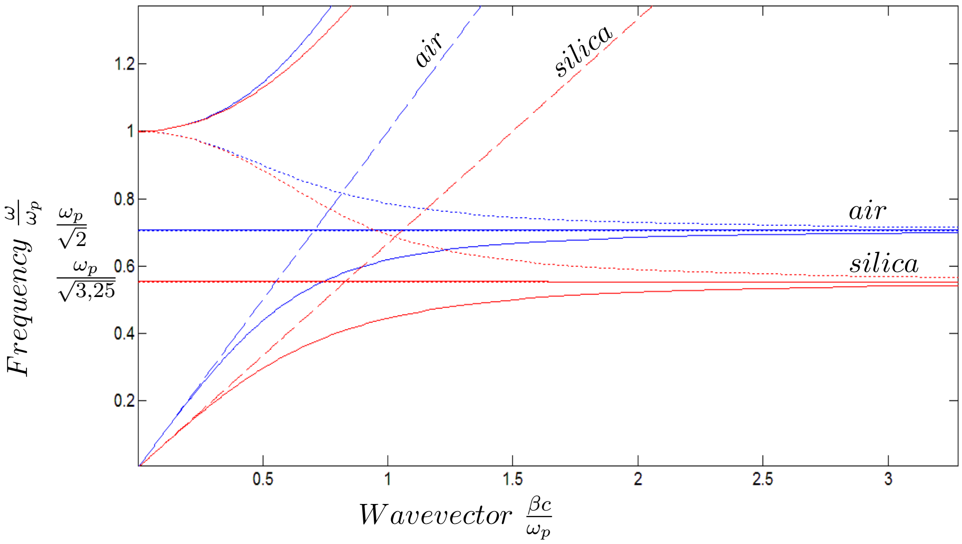

Figure 2.4: Dispersion relation of SPPs at the interface between a Drude metal and air (blue curve) and silica (red curve). Continuous lines: real part. Dotted lines: imaginary part. Dashed lines: light lines.

This graph shows that SPP excitations correspond to the part of the dispersion curves lying to the right of the respective light lines of air and silica [4]. For this reason, special phase-matching techniques such as grating or prism coupling are required for their excitation. Radiation into the metal occurs in the trasparency regime $\omega > \omega_p$. Between the regime of the bound and radiative modes, a frequency gap region with purely imaginary β prohibiting propagation exists.

For small wavevectors corresponding to low (infrared or lower) frequencies, SPP propagation constant is close to k_0 at the light line and the waves extend over many wavelengths into the dielectric space. In this regime, SPPs acquire the nature of a grazing-incidence light field, and are also known as *Sommerfeld-Zenneck waves.*

Large wavevectors are obtained approaching the characteristic *surface plasmon frequency*

$$\omega_{sp} = \frac{\omega_p}{\sqrt{1 - \epsilon_{r2}}} \tag{2.70}$$

Considering a model with neglegible damping of the conduction electron oscillation, the wavevector β goes to infinity as the frequency approaches ω_{sp}. The mode acquires electrostatic charachter, and it's known as the *surface plasmon.*

2.7 Excitation of Surface Plasmons

In the previous section it has been shown that SPP excitation occurs when $\beta > \frac{\omega n}{c}$. Hence, particular conditions must be satisfied to obtain excitation. There are various ways by which the excitation of surface plasmons can be obtained (i.e. by light or by electrons). Each method has particular reqirements, expressed in terms of metal surface characteristics. The most popular techniques are: *Prism Coupling* [9] and *Grating Coupling* [10].

2.7.1 Prism Coupling

Surface plasmon polaritons on a flat metal/dielectric interface cannot be excited directly by light beams since $\beta_{rad} > k_{rad_x}$, where k_{rad_x} is the wavevector of light on the dielectric side of the interface. The reason is that the projection along the interface of the momentum $k_{rad_x} = k \sin\theta$ (where θ is the angle of incidence of photons to the surface) is always smaller than the SPP propagation constant k_{SPP}.
However, phase-matching to SPPs can be achieved in a three-layer system consisting of a thin metal film sandwitched between two insulators of different delectric constants. SPPs happen because the wavevector of the light, travelling in a medium, is higher than in the air. Hence, in a dielectric, k_{rad_x} of a photon can equal k_{SPP} of SPP leading to excitation of SPPs.

The excitation is obtained by *ATR* (*attenuated total reflection*) method, in two cofigurations: *Kretschmann* and *Otto*.

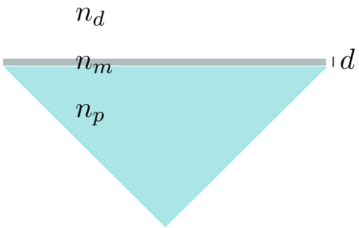

Figure 2.5: Kretschmann configuration

In *Kretschmann configuration* a high refractive index prism with refractive index n_p is interfaced with a metal-dielectric waveguide consisting of a thin metal film with permittivity ϵ_m and thickness d and a semi-infinite dielectric with a refractive index n_d (with $n_d < n_p$). When photons hit the metal film a part of the light is bounced back into the prism (the reflected part) and a part propagates in the metal. The transmitted part could be evanescent wave (a wave whose propagation direction is perpendicular to attenuation direction) in case of *TIR* (*total internal reflection*) which can excite surface plasmon polariton at interface metal/dielectric medium. However, the metal thickness needs to be low (less than 100 nm for light in visible and near infrared part of spectrum) in order to allow the penetration through

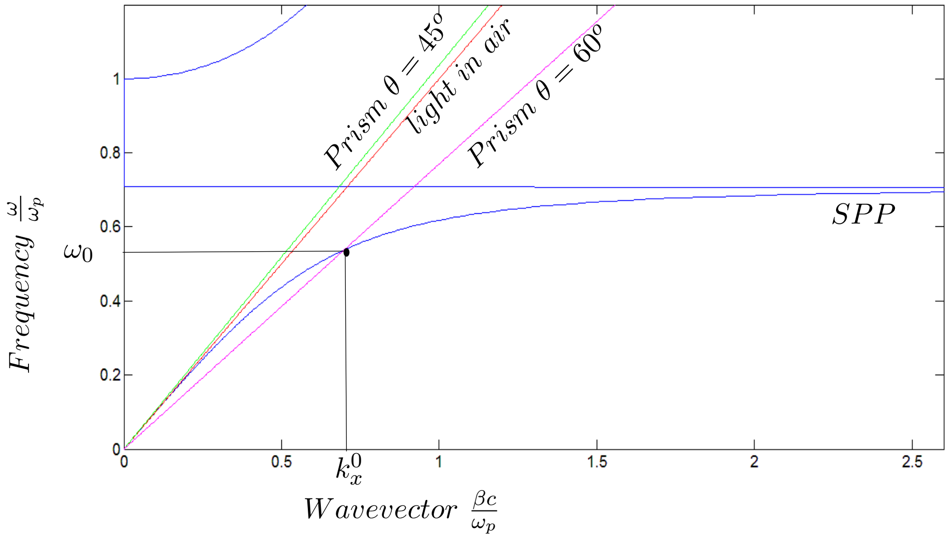

Figure 2.6: Dispersion relation of SPPs at the interface between a Drude metal and air (blue curve). Red line is the light line, green line is the light line in the prism with incidence angle of $\theta = 45^o$, magenta line is the light line in the prism with incidence angle of $\theta = 60^o$

the metal film.
It is necessary that

$$k_{rad_x} = k_{SPP} + \Delta\beta \tag{2.71}$$

in which k_{rad_x} is the wavevector of the incident light projected in the x-axis; k_{SPP} is the wavevector characteristic of the *plasmonic resonance* and $\Delta\beta$ accounts for the finite thickness of metal film and the presence of the prism. Two different analysis could be done taking/not taking in account the term $\Delta\beta$.

The simplest analysis, considering $\Delta\beta = 0$, results in

$$k_{rad_x} = k_{SPP} \tag{2.72}$$

where $k_{rad_x} = \frac{2\pi n_p}{\lambda_0}\sin(\theta)$ which is obtained considering the *Snell's law* ($n_p \sin(\theta) = n_m \sin(\theta_m)$). Thus, the condition for surface resonance can be rewritten in the following form:

$$\frac{\omega}{c}\sqrt{\epsilon_{r_p}}\sin(\theta) = \frac{\omega}{c}\sqrt{\frac{\epsilon_{r_m}\epsilon_{r_d}}{\epsilon_{r_m}+\epsilon_{r_d}}} \tag{2.73}$$

and, re-arranging

$$\sin(\theta) = \sqrt{\frac{\epsilon_{r_m}\epsilon_{r_d}}{\epsilon_{r_p}(\epsilon_{r_m}+\epsilon_{r_d})}} \tag{2.74}$$

The condition can be visualized graphically in Figure 2.6, where four curves (representing the wavevector as a function of frequency normalized to the plasma frequency ω_p) are plotted, considering $n_d = 1$ and $n_p = 1.5$:

- the blue one represents the surface polaritons

$$\frac{k_{SPP}c}{\omega_p} = \frac{\omega}{\omega_p}\sqrt{\frac{\epsilon_{r_d}(1-\frac{\omega_p^2}{\omega^2})}{1+\epsilon_{r_d}-\frac{\omega_p^2}{\omega^2}}}$$

- the red one represents the light wave travelling in the air

$$\frac{ck_{rad}}{\omega_p} = \frac{\omega}{\omega_p}$$

- the green one represents the projection on the x-axis of the wavevector of the light incident the prism with an angle $\theta = 45^o$

$$\frac{k_{rad_x}c}{\omega_p} = \frac{\omega}{\omega_p}\sqrt{\epsilon_{r_p}}\sin(45^o)$$

- the magenta one represents the projection on the x-axis of the wavevector of the light incident the prism with an angle $\theta = 60^o$

$$\frac{k_{rad_x}c}{\omega_p} = \frac{\omega}{\omega_p}\sqrt{\epsilon_{r_p}}\sin(60^o)$$

From the Figure 2.6 it is possible to see that in case of an incident angle of $\theta = 45^o$ there is no excitation of surface polaritons for any frequencies of light. In case of angle of incidence of $\theta = 60^o$ there is excitation because of the intersection between the two lines (k_x^0, ω_0), as stated in Section 2.6. In this case, at a certain value of frequency$\frac{\omega}{\omega_p}$, $\theta = 60^o$ is the position of the maximum of resonance.

The same graph can be used in an angular scanning analysis: once chosen a certain frequency of the laser $\frac{\omega}{\omega_p}$ there is only one point on the curve which represents the maximum of resonance. It is obtained at a certain incidence angle. While scanning, the line curve (green, it represents the projection of the wavevector of the incident light) rotates around the origin of the axes. In Figure 2.7, to obtain the excitation an incident angle higher than $\theta = 60^o$ is necessary.

A more detailed analysis should consider the term $\Delta\beta$, as well. It accounts for the finite thickness of the metal film and the presence of the prism, not considered previously [9, p. 12]. In order for the coupling between the evanescent wave and the surface plasmon to occur, the propagation constant

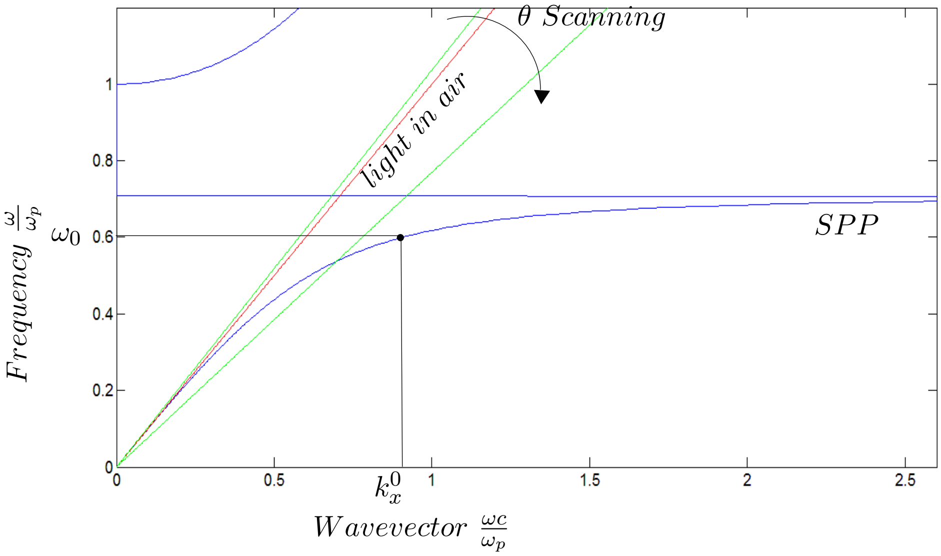

Figure 2.7: Dispersion relation of SPPs: once the frequency has been chosen, scanning the angle makes the green line rotate around the origin of the axis.

of the evanescent wave k_{rad_x} and that of the surface plasmon $k_{SPP} + \Delta\beta$ must be equal:

$$k_0 n_p \sin(\theta) = Re\left[k_0\sqrt{\frac{\epsilon_{r_d}\epsilon_{r_m}}{\epsilon_{r_d}+\epsilon_{r_m}}} + \Delta\beta\right] \tag{2.75}$$

which can be also written in terms of effective index:

$$n_p \sin(\theta) = Re\left[\sqrt{\frac{\epsilon_{r_d}\epsilon_{r_m}}{\epsilon_{r_d}+\epsilon_{r_m}}}\right] + \Delta n_{ef}^{SP} \tag{2.76}$$

where $\Delta n_{ef}^{SP} = Re\left[\frac{\Delta\beta\lambda}{2\pi}\right]$
The term $\Delta\beta$ describes the effect of the prism and, as a complex quantity, has a real part, which perturbs the real part of the propagation constant of a surface plasmon on the interface of semi-infinite dielectric and metal, and an imaginary part, which causes an additional damping of the surface plasmon due to the outcoupling of a portion of the field into the prism [10, p. 31]. This damping is due to the radiation emitted from the SPs at the interface metal/dielectric back into the prism in the direction of the reflected beam.

To analyze the effect of $\Delta\beta$ on reflectivity, let's consider a 3-layers system (Figure 2.8). In this case,the *amplitude Fresnel coefficient* can be written is the following form:

$$r_{pmd} = \frac{r_{pm} + r_{md}e^{j2k_{2_x}d}}{1 + r_{pm}r_{md}e^{2jk_{2_x}d}}$$

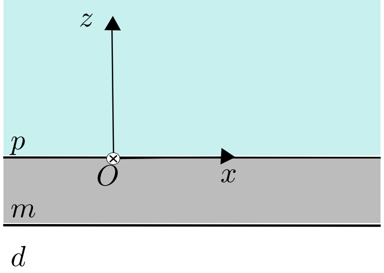

Figure 2.8: 3 layer model

where r_{ij} is the *amplitude Fresnel coeffient*, calculated appositely for TM or TE polarization of the incident light, between layers ij, $k_{i_x} = \sqrt{k_0^2\epsilon_i - k_{i_z}^2}$ and d is the thickness of the intermediate material (the metal in *Kretschmann configuration*). The *power reflection coefficient* can be written in the form

$$R = |r_{pmd}|^2$$

When $|Re\left[\epsilon_{r_m}\right]| \gg 1$ and $|Re\left[\epsilon_{r_m}\right]| \gg |Im\left[\epsilon_{r_m}\right]|$ the reflectivity can be approximated in the region of the resonance by the *Lorentzian type relation* [11]:

$$R = 1 - \frac{4Im\left[k_{SPP}\right]Im\left[\Delta\beta\right]}{(k_{rad_x} - Re\left[k_{SPP} + \Delta\beta\right])^2 + (Im\left[k_{SPP}\right] + Im\left[\Delta\beta\right])^2} \tag{2.77}$$

where

$$k_{SPP} = \frac{\omega}{c}\sqrt{\frac{\epsilon_{r_m}\epsilon_{r_d}}{\epsilon_{r_m} + \epsilon_{r_d}}} \tag{2.78}$$

$$\Delta\beta = r_{12}e^{j2k_{m_x}d}2\frac{\omega}{c}\left(\frac{\epsilon_{r_m}\epsilon_{r_d}}{\epsilon_{r_m} + \epsilon_{r_d}}\right)^{\frac{3}{2}}\frac{1}{\epsilon_{r_d} - \epsilon_{r_m}} \tag{2.79}$$

The reflectivity under the *Lorentzian approximation* can be also rewritten as

$$\begin{aligned} R = 1 - \frac{4\Gamma_i\Gamma_{rad}}{(n_p\sin\theta - n_{ef}^{SP})^2 + (\Gamma_i + \Gamma_{rad})^2} = \\ = 1 - \frac{4xy}{(A)^2 + (x+y)^2} \end{aligned} \tag{2.80}$$

where:

- $\Gamma_i = Im\left[k_{SPP}\right]\frac{\lambda}{2\pi}$ is the internal absorption. It consists in excitation by electromagnetic field of electron-hole pairs at the Fermi level. The de-excitation produces phonons, which are lattice vibrations (and thus causes heating), and photoelectrons if $\hbar\omega >$ work function (with the exception of silver, which produces only phonons unless there is a change in work function[12]);

- $\Gamma_{rad} = Im\left[\Delta\beta\right]\frac{\lambda}{2\pi}$ is the radiation loss. It is caused by SPs evanescent wave which creates a plane wave into the prism (it is a characteristic for an asymmetric two-interface system like this).

The depth of the dip reaches the maximum when

$$\left(\frac{\partial R}{\partial \Gamma_i}, \frac{\partial R}{\partial \Gamma_{rad}}\right) = (0, 0) \tag{2.81}$$

$$\left(\frac{\partial R}{\partial x}, \frac{\partial R}{\partial y}\right) = \left(\frac{4y(A^2 - y^2 + x^2)}{A^2 + (x+y)^2}, \frac{4x(A^2 - x^2 + y^2)}{A^2 + (x-y)}\right)$$

$$\left(4y(A^2 - y^2 + x^2), 4x(A^2 - x^2 + y^2)\right) = (0, 0)$$

$$x = y \;\; \rightarrow \;\; \Gamma_i = \Gamma_{rad} \tag{2.82}$$

Hence, the maximum depth is reached when the radiation (Γ_{rad}) and absorption losses (Γ_i) are equals. The minimum condition $\Gamma_i = \Gamma_{rad}$ is satisfied only for a single thickness of the metal film. In this case, called *Optimum Coupling*, the angular half-width of the dip $\Delta\theta_{1/2}$ (the angular width of the dip at R=0.5) can be expressed as

$$\Delta\theta_{1/2} = \frac{4\Gamma_i}{n_p \cos\theta} \tag{2.83}$$

where θ is the coupling angle.
Simulating the system response with the technique described in Chapter 3, it is possible to see the behaviour of five different thicknesses of the metal film (Figure 2.9).

In the simulation performed the following parameters are considered: a laser with $\lambda = 633$ nm, a prism of $n_p = 1.5$ and silver metal medium with $n_m = \sqrt{-17 - j0.7}$, $n_d = 1$. The five curves represent five different thicknesses of metal:

- the magenta one is the simulated behaviour for a metal thickness of $d = 25$ nm;
- the blue one is the simulated behaviour for a metal thickness of $d = 35$ nm;
- the red one is the simulated behaviour for a metal thickness of $d = 52.5$ nm;

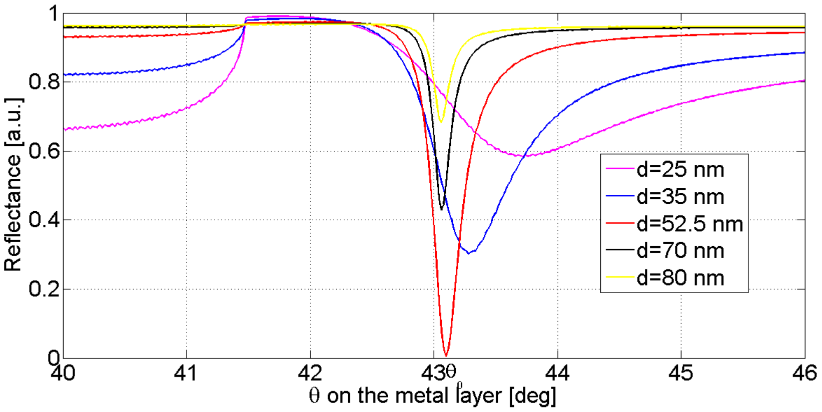

Figure 2.9: Simulation of the system in case of 5 different thicknesses of the metal

- the black one is the simulated behaviour for a metal thickness of $d = 70$ nm;
- the yellow one is the simulated behaviour for a metal thickness of $d = 80$ nm.

From this simulation it is possible to observe that the resonant angle decreases with the increasing of the thickness: it reaches the value $\theta_{SP_0} = 43.4^o$ which corresponds to a surface plasmon propagating along an isolated metal dielectric waveguide ($d \to \infty$, $\Delta\beta = 0$). The thickness of the metal film influences the depth of the reflectivity minimum, as well. The strongest excitation of SPP ($R \approx 0$) occurs when $d \approx 52.5$ nm.

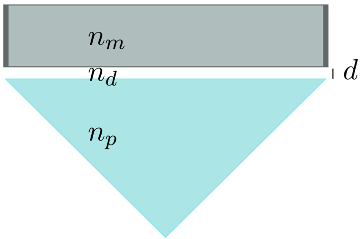

Figure 2.10: Otto configuration

In *Otto configuration* a high refractive index prism with refractive index n_p is interfaced with a dielectric-metal waveguide consisting of a thin dielectric film with refractive index n_d ($n_d < n_p$) and thickness d, and a semi-infinite metal with permittivity ϵ_m. In this configuration, in case of an incident angle causing TIR, the light produces an evanescent wave propagating along the interface between the prism and the dielectric film. If the

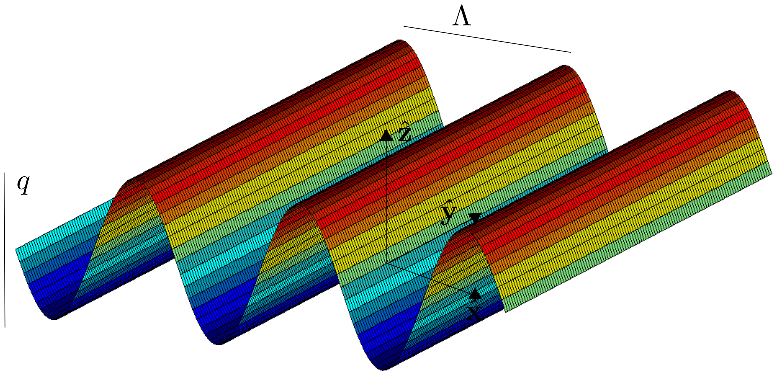

Figure 2.11: Example of grating surface - sinusoidal in x-direction

dielectric layer is enough thin (typically few microns), the evanescent wave and a surface plasmon at the dielectric-metal interface can couple.
In order to get the coupling, the propagation constant of the evanescent wave and that of the surface plasmon need to be equal.

2.7.2 Grating Coupling

This technique is based on the diffraction of light on a diffraction grating. A diffraction grating is an optical device in which the relative permittivity varies periodically across the surface, and whose period is of the order of the wavelength of the light. This variation leads to localized phase changes in the impinging field, resulting in constructive or destructive interference of the waves in the far-field.

Different geometries of grating structure have been analyzed in literature. The simplest structure is a 1 dimensional periodic structure, whose section can be a sine or a square, for instance. In literature can be found examples of 2D grating structure (i.e. [13]); however, the analysis isn't as simple as the 1D case.

Supposing a 1D surface like that in Figure 2.11, choosing the coordinate system so that x is parallell to the unit lattice vector of the periodic structure and y is parallell to the grooves, assuming the incident light lies in the xz plane, the wavevector of the diffracted light $\mathbf{k}_m$ is [14]:

$$\mathbf{k}_m = \mathbf{k} + m\mathbf{G} \tag{2.84}$$

where $\mathbf{k}$ is the wavevector of the incident light, m is an integer and denotes the diffraction order, $\mathbf{G} = \frac{2\pi}{\Lambda}\hat{\mathbf{x}}$ is the *grating vector* and Λ is the *grating*

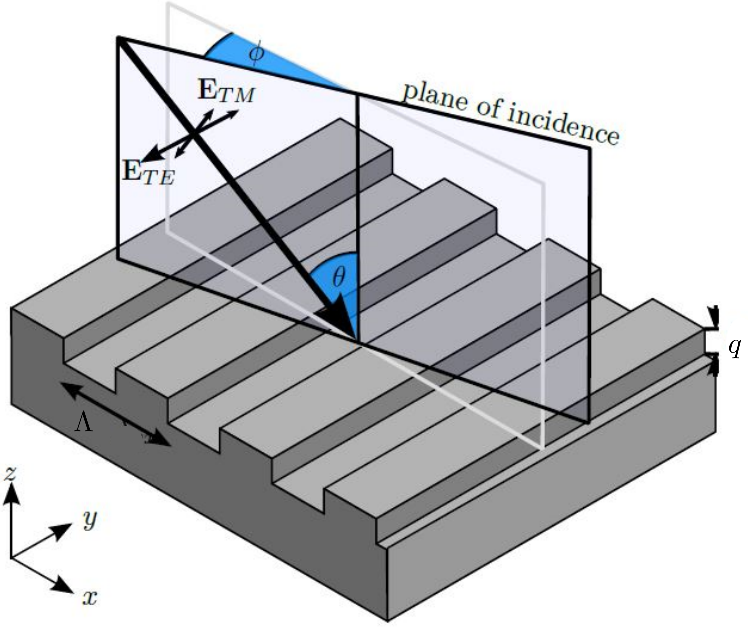

Figure 2.12: 1D square grating structure

step. Therefore, for the SPPs to occur, it's necessary that

$$Re\left[k_{SPP} + \Delta\beta\right] = k_x + m\frac{2\pi}{\Lambda} \tag{2.85}$$

where $\Delta\beta$ considers the effects of grating and becomes zero when $q \to 0$.

In a more general condition, when **k** doesn't lie in xz plane (as represented in Figure 2.12)

$$\mathbf{G} = \begin{pmatrix} m\frac{2\pi}{\Lambda} \\ 0 \\ 0 \end{pmatrix}$$

and

$$\mathbf{k} = \begin{pmatrix} \frac{2\pi}{\lambda} n_d \sin\theta\cos\phi \\ \frac{2\pi}{\lambda} n_d \sin\theta\sin\phi \\ -\frac{2\pi}{\lambda} n_d \cos\theta \end{pmatrix}$$

leading to the following condition for the excitation (ignoring the term $\Delta\beta$)

$$\mathbf{k}_{SPP} = \begin{pmatrix} \frac{2\pi}{\lambda} n_d \sin\theta\cos\phi \\ \frac{2\pi}{\lambda} n_d \sin\theta\sin\phi \\ -\frac{2\pi}{\lambda} n_d \cos\theta \end{pmatrix} + \begin{pmatrix} m\frac{2\pi}{\Lambda} \\ 0 \\ 0 \end{pmatrix} \tag{2.86}$$

and, considering that $\mathbf{k}_{SPP}$ lies in the plane xy

$$\begin{pmatrix} k_{SPP_x} \\ k_{SPP_y} \\ 0 \end{pmatrix} = \begin{pmatrix} \frac{2\pi}{\lambda} n_d \sin\theta\cos\phi \\ \frac{2\pi}{\lambda} n_d \sin\theta\sin\phi \\ -\frac{2\pi}{\lambda} n_d \cos\theta \end{pmatrix} + \begin{pmatrix} m\frac{2\pi}{\Lambda} \\ 0 \\ 0 \end{pmatrix} \tag{2.87}$$

By calculating the module it is possible to obtain the *Surface Plasmon Condition*:

$$|\mathbf{k}_{SPP}|^2 = k_{SPP_x}^2 + k_{SPP_y}^2 =$$

$$= n_d^2 \left(\frac{2\pi}{\lambda}\right)^2 \sin^2\theta + 2n_d \frac{2\pi}{\lambda} m \frac{2\pi}{\Lambda} \sin\theta\cos\phi + m^2 \left(\frac{2\pi}{\Lambda}\right)^2 \tag{2.88}$$

This analysis is called *Wavevector model* and it's used to find out the position (in terms of θ and ϕ) in which the SPPs occur.

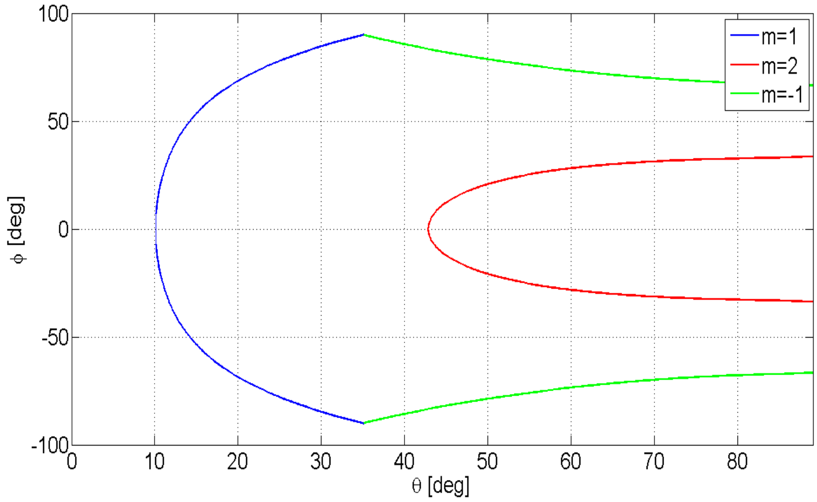

Figure 2.13: Position in which SPPs excitation occur. Simulation using the *Wavevector model*, with $n_d = 1$ (air), $\lambda = 633$ nm, $\Lambda = 740$ nm and $\epsilon_m = \sqrt{-17 - j0.7}$ (silver). One-dimensional grating.

Using the software MATLAB it's possible to perform a simulation of (2.88), considering the following parameters: $n_d = 1$ (air), $\lambda = 633$ nm, $\Lambda = 740$ nm and $n_m = \sqrt{-17 - j0.7}$ (which is the silver surface). The result is represented in Figure 2.13.

It should be noticed that this analysis does not take in account of the non-zero thickness of the grating structure, leading to an approximative result.

Diffraction gratings aren't used only for SPPs: it is a useful way to obtain polarization conversion. The polarization conversion occurs when the surface grating is arranged so that the scattering vector does not lie in the plane of incidence of the light radiation (i.e. in Figure 2.12, when a TM polarized light hits the surface and the outcoming light does not lie on the plane of incidence) [15].

2.7.3 Grating in Prism Coupling

The grating structure explained in the previous Section can be also used in prism coupling. In this case, there are two interfaces at which the plasmonic excitation can occur:

- the metal/dielectric interface;
- the metal/prism (or substrate, if we consider a real device with a supporting layer) interface.

This condition is depicted in Figure 2.14, in which a grating metal layer is coupled with a high refractive index prism. The two interfaces lead to two different plasmonic excitation:

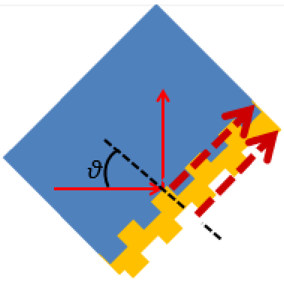

Figure 2.14: Grating structure on prism coupling. Two plasmons excited: one at the metal/dielectric interface, one at the metal/prism (or substrate for the metal) interface.

- the metal/prism (or substrate) interface causes a *Grating peak* whose condition are given by the *wavevector analysis* explained in Section 2.7.2. The plasmon wavevector $\mathbf{k}_{SPP}$ depends on $\epsilon_{prism/substrate}$ and ϵ_{metal}, making this grating peak independent on the dielectric material on the device;
- the metal/dielectric interface causes a *Kretschmann peak* whose excitation condition are given by Equation (2.74). $\mathbf{k}_{SPP}$ in this case depends on ϵ_{metal} and $\epsilon_{dielectric}$, making it sensitive to dielectric on the metal device (in Figure 2.14 air is considered as the dielectric).

When the metal layer is functionalized (covered with a biomaterial) to use it as a biosensor, this change involves the *Kretschmann peak* only, leaving

unaltered the *grating peak*. Therefore, because of this “fixed” value for the grating peak, it is possible to consider it as a *reference value* for precise measurements when developing a SPR biosensor [16] [17].
In Figure 2.15 the position of resonance peaks for a grating device on a prism is obtained. In this model, we considered a grating step $\Lambda = 740$ nm, a prism of $n_p = 1.51$ and a substrate of $n_{substrate} = 1.586$. The dielectric considered is the air $n_{dielectric} = 1$.
The positions of the grating peak are plotted in terms of ϕ and θ angles using the *wavevector model* (blue and green curves); Equation (2.74) is used to calculate the Kretschmann peak position (magenta line).

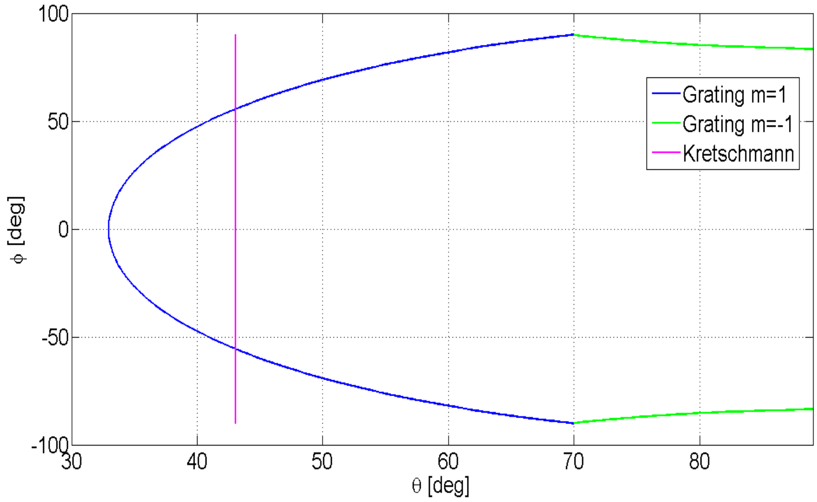

Figure 2.15: Position in which SPPs excitation occur. Simulation using the *Wavevector model*, with $n_d = 1$ (air), $\lambda = 633$ nm, $\Lambda = 740$ nm and $n_m = \sqrt{-17 - j0.7}$ (silver), $n_p = 1.51$ and $n_{substrate} = 1.586$. One-dimensional grating.

Chapter 3

SPR Sensors: Introduction, Measurement Set-up and Numerical Simulation

As seen in the previous Chapter, SPPs excitation occurs only under certain conditions of incident angle, wavelength and materials refractive indexes. This led to use SPPs excitation to probe processes at the surfaces of metals [18] and to detect gases [19]. Since then (1980), SPR sensors, which are "*converters that measure a physical quantity and convert it into a signal which can be read by an observer or by an (today mostly electronic) instrument*", have been developed. They consist of an optical system, a sensor data acquisition and a processing system.
Light coming from a source (i.e. a laser) excites SPPs leading to an output light wave with an encoded SPR signal. This output light can be detected and processed to obtain a sensor output.

This chapter is focused on the description of SPR sensors, from a theoretical point of view, with their main characteristics and classifications, and from a pratical point of view, with the presentation of the state of art of development of SPR Biosensor. The SPR sensors here presented are mostly developed in the field of food safety, which is the field involved by this thesis, with a particular attention on the type of molecule recognised.
Another section examines the set-up for the LUXOR (Laboratory for Ultraviolet and X-ray Optical Research) Kretschmann bench of CNR-INF Institute of Padova, presenting materials and methods involved in the measurement results obtained in Chapter 4. A simulation MATLAB program implemented to predict the behaviour of the Kretschmann bench is then explained.

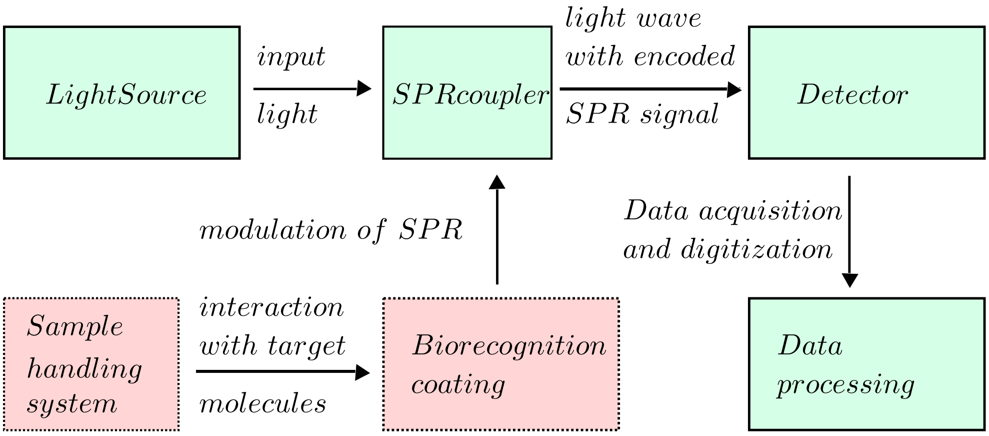

Figure 3.1: Scheme of an SPR (bio)sensor [10, p. 96]

3.1 Introduction to SPR Biosensors

SPR sensors are usually used to measure changes in the refractive index n_d of the dielectric. When the refractive index of the dielectric material changes, e.g., a second a layer is grown on it, there is a change in the conditions (in terms of λ, θ, polarization...) for SPPs excitation to occur.
In SPR biosensors, the layer grown on the metal has biological origin. It consist in a biomaterial which has the chemical property of forming a bond with the metal surface and therefore changing the dielectric characteristics like refractive index - hence changing the conditions for SPPs excitation.

However, when analysing the measured values, it should be remebered that SPR is a real instrument, with all the limitations of real measurement systems like *repeatability*, *riproducibility*, *sensitivity* and *resolution* which define the accuracy of the measurement system.

- the *repeatability* is the ability of the instrument to provide the same output when measuring the same value of the measurand using the same settlment of the bench over time. It is sometimes expressed as a percentage of full range.
  This property depends strictly on the characteristics of the bench: when measuring a value $X_{measured}$, it differs from the true value X_{true} by the random error e and the error due to assignable causes S [20]

  $$X_{measured} = X_{true} + S + e \tag{3.1}$$

  - the random error e is due to *random causes*, which are statistical fluctuations. They can be modeled as random variable whose mean is zero: a useful representation is the Gaussian distribution function (because of the Central Limit theorem) where, ignoring

S, $E[e] = 0$

$$E[X_{measured}] = X_{true} + E[e] = X_{true} \tag{3.2}$$

$$var(X_{meaured}) = var(e) \tag{3.3}$$

  - the systematic error S is due to *assignable causes*, also known as systematic errors, which are inaccuracies consistently in the same direction. The value of S is usually unknown unless other information is obtained (i.e. temperature or umidity variations).

    They can be eliminated or reduced by a re-calibration of the system.

  Once these two errors have been analyzed, it is possible to characterize the instrument uncertainty: a *Confidence interval* has been obtained. It is represented as an interval $[X - U_x, X + U_x]$ in which it's possible to find the measured value with a probability of 95-99%.

- *riproducibility* is the ability of the instrument to provide the same result when performed by other operators or mesurement benches.

- *sensitivity* is the ratio of the change in sensor output to the change in the measurand. However, discussing the sensitivity of SPR is always difficult: it depends on what is consider as the measurand value. Indeed, sensitivity can be referred to the change in the refractive index of the fluid medium RIU; it can be referred to surface coverage (if it's important the dection of molecular binding taking place on a sensor surface) in terms of mass, e.g. $\frac{pg}{mm^2} = RU$ (resonance unit of response unit); it can be referred to molar concentration as well.
  If the sensitivity is referred to the refractive index of the fluid medium, it is possible to consider the sensitivity as:

$$S = \frac{\partial Y}{\partial c} = \frac{\partial Y}{\partial n_{eff}} \frac{\partial n_{eff}}{\partial n} = S_1 S_2 \tag{3.4}$$

  where Y is the measurand, n_{eff} is the effective refractive index (from the dispersion relation $\beta = \frac{\omega}{c}\sqrt{\frac{\epsilon_{r_d}\epsilon_{r_m}}{\epsilon_{r_d}+\epsilon_{r_m}}} = \frac{\omega}{c}\left(n_{eff} + i\eta\right))$, n is the refractive index.
  The first term S_1 describes the sensitivity of the sensor output to the effective index of a surface plasmon and depends on the method of excitation and modulation used. The second term S_2 describes the sensitivity of the effective index of a surface plasmon to the refractive index and is independent of the modulation method and method of excitation.

In case of SPR prism coupling sensor with angular modulation (as in case of Kretschmann bench), from equation (2.76), considering $\Delta\beta = 0$:

$$\Delta n_{eff} = n_p \sin\theta - n_{eff} = 0 \tag{3.5}$$

differentiating

$$n_p \cos\theta d\theta - dn_{eff} = 0 \tag{3.6}$$

and rearranging

$$\frac{d\theta}{dn_{eff}} = \frac{1}{n_p \cos\theta} \tag{3.7}$$

and, remembering that $\cos\theta = \sqrt{1 - \sin^2\theta} = \sqrt{1 - \frac{n_{eff}^2}{n_p^2}}$ it is possible to get the value for

$$S_1 = \frac{d\theta}{dn_{eff}} = \frac{1}{\sqrt{n_p^2 - n_{eff}^2}}. \tag{3.8}$$

Hence, the sensitivity of the instrument is strictly dependent on the difference between the refractive index of the prism and the effective index of the surface plasmon.
The value S_2 can be calculated using the perturbation theory [10], obtaining the total sensitivity:

$$S_\theta = S_1 S_2 = \frac{\epsilon_{m_1}\sqrt{-\epsilon_{m_1}}}{(\epsilon_{m_1} + n^2)\sqrt{\epsilon_{m_1}(n^2 - n_p^2) - n^2 n_p^2}} \tag{3.9}$$

where ϵ_{m_1} is the real part of the permittivity of metal, n is the bulk refractive index and n_p is the prism refractive index. It should be noticed that ϵ_{m_1} depends on the wavelength of the laser used: in Figure 3.2 the sensitivity of a prism coupling SPR is plotted as a function of the wavelength. $n_p = 1.51$ and $n = 1.32$ are considered. Refractive index values are collected from [21].
From the figure it is clear that the sensitivity for a prism coupler SPR decreases with an increasing wavelength. For example, at $\lambda = 633$ nm and $n = 1.32$ the sensitivity for SPR prism coupling sensor should reach the value of $\frac{d\theta}{dn} = 120.05 \frac{deg}{RIU}$.

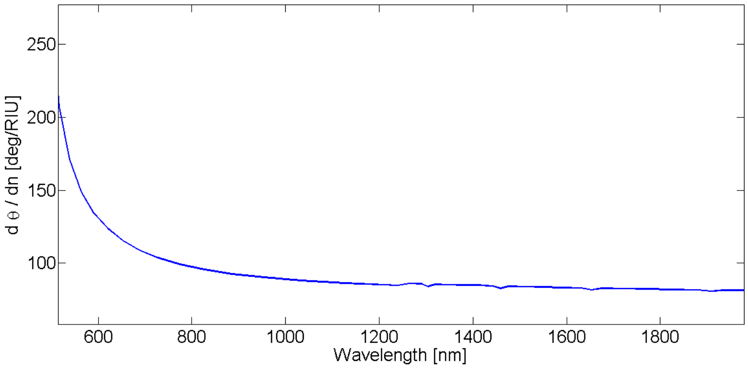

Figure 3.2: Sensitivity for prism coupling SPR as a function of wavelength. $n_p = 1.51$, $n = 1.32$, Silver metal

The grating coupler sensor sensitivity could be analized as well. Even if the grating coupler presents a sensitivity which depends on two parameters (the wavelength and the diffraction order), the resulting sensitivity is comparable with the prism coupling system [22].
In literature various ways to improve sensitivity are reported: it is possible to use nanoparticles (silver or gold) (for example [23]) or it is possible to enhance sensitivity by controlling the azimuthal angle (for grating coupling only) [24].

- *linearity* when there is a linear (approximated) relationship between the measurand and the sensor output. It is a desirable feature because these sensors require fewer calibration points to produce an accurate sensor calibration. However, most of them are not linear; therefore a precise calibration is strictly required.

- *accuracy* is the property for which the measured value and the real value are close each other. It can be expressed in absolute terms or in a percentage form.

- *resolution* is the smallest change in the bulk refractive index that produces a detectable change in the sensor output. It depends on the level of uncertainty of the output, therefore depends on the noise. Noise source can be originated by:
  - fluctuations in the light intensity: this noise is proportional to the intensity and therefore its standard deviation can be given as $\sigma_L = \sigma_L^{rel} I$, where σ_L^{rel} is the relative (intensity independent) standard deviation and I is the measured light intensity;
  - statistical property of light (shot noise), which is associated with random arrival of photons on a detector and corresponds to a random production of photoelectrons. Photons produced by a laser

  obeys to Poisson statistics, producing a shot noise whose standard deviation $\sigma_S = \sigma_S^{rel}\sqrt{I}$, where σ_S^{rel} is the relative standard deviation;

  - noise conversion of light intensity into photoelectrons by the photodiode and the supporting cicuitry, a noise whose standard deviation σ_D is independent on the detected light intensity.

The resulting noise is obtained by superimposition of all these components, leading to the following noise:

$$\sigma_I(I) = \sqrt{I^2(\sigma_L^{rel})^2 + I(\sigma_S^{rel})^2 + \sigma_D^2} \tag{3.10}$$

This theoretical result can be used to obtain an expression [25] for the refractive index resolution:

$$\begin{aligned}\sigma_{RI}^{(all)} &= \frac{Kr}{\sqrt{N}} \frac{(\Gamma_i + \Gamma_{rad})^3}{\Gamma_i \Gamma_{rad}} \left(\frac{\partial n_{eff}}{\partial n}\right) \frac{\sigma_{I(max)}}{I_0} = \\ &= \frac{Kr}{\sqrt{N}} \frac{(\frac{\Gamma_i}{\Gamma_{rad}} + 1)^3}{(\frac{\Gamma_i}{\Gamma_{rad}})^2} \frac{\epsilon_{m_2} n^3}{2(\epsilon_{m_1})^2} \frac{\sigma_{I(max)}}{I_0}\end{aligned} \tag{3.11}$$

where K is the noise distribution factor (a number which depends on the SPR sensor type), r is the noise correlation factor, I_0 is a portion of the intensity of the incident light generating surface plasmon which corresponds to one detector, $\Gamma_i = Im[k_{SPP}]\frac{\lambda}{2\pi}$ is the internal absorption, $\Gamma_{rad} = Im[\Delta\beta]\frac{\lambda}{2\pi}$ is the radiation loss (see Chapter 2), $\sigma_{I(max)}$ is the standard deviation of noise of the highest intensity involved in the data analysis and N is the total number of light intensities averaged in time and space.
This formula states a theoretical limit to the instruments used nowadays - these limits are predominantly determined by properties of the surface plasmon phenomenon and the present state of development of optical components. Future improvement of SPR sensors limits depends mostly on the development of detectors of light intensity with a higher signal to noise ratio, hence by increasing the size of the detector or by increasing the frame-rate and the number of temporally averaged intensities [25].

- *dynamic range* describes the span of the values of the measurand that can be measured by the sensor. It describes a range of values of the refractive index of the sample that can be measured with a specified accuracy. For biosensors this value defines the range of concentration of analyte that can be measured.

- *limit of detection* or *LOD*, defined by the International Union of Pure and Applied Chemistry [10], is the concentration of analyte c derived from the smallest measure Y that can be detected with reasonable certainty. The value of Y_{LOD} is given by

$$Y_{LOD} = Y_{blank} + m\sigma_{blank} \tag{3.12}$$

where Y_{blank} is the mean of the blank measures (with no analyte), σ_{blank} is the standard deviation of the blank measures and m is the desired confidence level. Remembering that $c_{blank} = 0$ (the concentration c of the analyte is zero in the blank case),

$$c_{LOD} = \frac{1}{S(c=0)} m\sigma_{blank} \tag{3.13}$$

where $S(c=0) = \frac{d\theta(c=0)}{dc}$ is the sensitivity of the sensor (with angular modulation) to variation of the analyte concentration. It should be noticed that the using this definition of LOD it's possible to recognize only false positives, which in effect makes the probability of a false negative equal to 50% [26].

SPR sensors can be classified depending on their characteristics, e.g., light modulation. In literature SPR with either angular, wavelength, intensity, phase or polarization modulation are reported: each one of this sensors uses a different modulation system. An angular modulation sensor, for instance, works keeping fixed all set-up parameters with the exception of the angle θ. Hence, performing an angular scanning (varying the incident angle in a certain range of values) can result in a characteristic reflectance curve. Another classification of SPR sensors is the distinction between direct or indirect. In direct SPR sensors, the measurand (typically refractive index) modulates characteristics of the light directly. In indirect SPR sensors, the measurand modulates an intermediate quantity which then modulates the light characteristics.

3.2 Surface Immobilization

One of the aims of SPR sensor is to recognize the presence of biomolecules (proteins, DNA, peptides...) from a sample. To perform this, it's necessary to find a way to fix these molecules to the metal, so that the SPR sensor, which measures the variation of the refractive index of the dielelectric material, is able to recognize them. This process of modyfing the surface is called *Immobilization procedure*: it is caused by chemical bounds created between molecules and metal.

Even if metal substrates such as gold and silver show a high tenedency for spontaneous adsorption of biological molecules, it is difficult to select exactly the desired ones. Hence, it is reccomended to coat the metallic surface with a medium which can work as a “glue” for the target molecules and which can minimize the non-specific absorption, leading to a selection of the desired molecules.

A good way to fix only the desired molecule to the metal surface is to use a specific antibody immobilized to the metallic surface. However, these antibodies will reduce their bioactivity [10] if they are bounded directly to the metal surface; hence, a layer of a material able to fix to metal and to the antibodies is needed. The fixation of this material to the metallic surface is called *functionalization procedure.*

3.2.1 Self-Assembled Monolayers and the PEG Case

The most successful method to functionalize the metallic surface consists in using *Self-assembled monolayers* (SAM): they provide a convenient, flexible and simple system with which to tailor the interfacial properties of metals, metal oxides and semiconductors. They consist in organic assemblies formed by the adsorption of molecular constituents from solution; the adsorbates organize spontaneously into crystalline (or semicrystalline) structures.

The molecules or ligands which form SAMs have a chemical functionality with a specific affinity for a substrate: for this reason it is possible to consider different materials that bind to different metals, metal oxides and semiconductors [27].

The widest known molecules for coating the surface are thiol- or disulfide molecules. In literature, lots of cases can be found; gold, the first surface on which SAM was reported [28], is the reference metal for the following five characteristics:

- gold is easy to obtain as a thin film by physical vapor deposition, sputtering or electrodeposition;
- gold is easy to pattern by a combination of lithographic tools (i.e. photolithography);
- gold is a resonably inert metal - it does not oxidize or react with O_2 or with most chemicals;
- gold binds thiols with a high affinity and does not react unusually with them;
- gold is compatible with cells - cells can adhere and live on gold surfaces without evidence of toxicity.

Silver is also a well-studied surface: it gives high quality SAMs with a simple structure. However, it oxidizes readily in air, it is toxic to cells and the knowledge about the reactions for forming SAMs from organosulfur compounds is still quite unknown - the structural details between this metal (like copper and palladium, for example) and the monolayer are only understood

in qualitative levels.
What it is clear is that SAMs molecules tend to adopt structures that are similar to simple adlayer formed by elemental sulfur on that metal.

A good SAM is obtained from a modified version of *PEG - poly(ethylene Glycol)* (also known as *PEO - poly(ethylene oxide)*), which is the *thiolated PEG*. It is a polymer of considerable technical importance: it is usually used to coat surfaces in order to prevent proteins or other macromolecular material from depositing on the surface [29]. It consists in three parts:

- the thiol- molecule, which is able to fix itself to the metal surface by a chemical reaction, forming a covalent bond with the metal;
- the $O - CH_2 - CH_2$ chain, whose length depends on the molecular weight;
- the $-OH$ end, substituted by the X functional group used to bond the antibody (in case of this Thesis, $-COOH$).

From the point of view of the kinetics of the formation of monolayers, the process is still not completely understood [29]. Several groups have studied the kinetic for assembly of alkanethiolates on gold (for example [30]), which can be considered as a reference for all thiol- molecules. All these works indicate that greater than 90% of the monolayer forms quickly - within minutes for milli-molar solutions of thiol- and the remainder forms more slowly over hours. The kinetics for the initial, rapid assembly of the monolayer are probably dominated by the interaction between the thiolated and gold substrate and gives a monolayer that is locally ordered but contains defects. It is presumed that the second, slower phase of assembly involves the reordering of alkanethiolates on the surface and transfer of alkanethiol molecules from solution to the remaining vacant sites on the gold substrate.

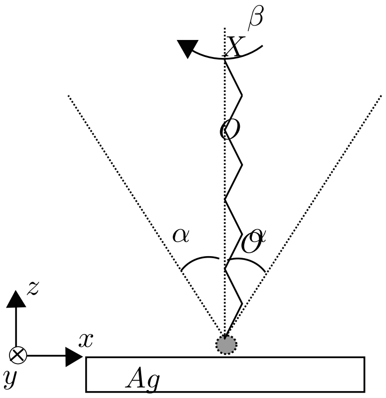

Figure 3.3: PEG molecule on metallic sufrace: α is the tilt angle, β is the twist angle

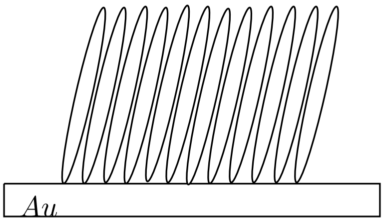

Figure 3.4: Representation of a generic SAM on the surface of gold. The alkyl chains are close-packed and tilted approximately 30^o from the normal to the surface. Properties of SAM are controlled by changing the length of the alkyl chain and terminal functional group X

When fixed to the metallic surface, the PEG structure can be represented as in Figure 3.3. While the thiol- molecule is fixed to the metal, the long chain can assume a particular geometric arrangement on the surface. A simple single-chain model is a good way to describe the behaviour of the PEG molecule: α defines the angle of tilt for the linear backbone of the molecule away from the surface normal; β defines the angle of rotation about the long axis of the molecule.

When using PEG-thiol, it should be remembered that SAMs suffers time degradation. Studies [31] reported that PEG-thiol SAMs on gold degrade in room air in less than two weeks by thiol-Au bond oxidation, leading to the desorbation of more than half of the PEG molecules.

3.2.2 PEGylation

To couple PEG to a molecule (i.e. polypeptides, polysaccarides, polynucleotides and small organic molecules) it is necessary to activate the PEG by preparing a derivative of the PEG having a functional group at its end. The functional group X, as said in the previous Section, is chosen based on the type of available reactive group on the molecule that will be coupled to the PEG. For proteins, for example, typical reactive amino acids include lysine, cysteine, histidine, N-terminal amino group and C-terminal carboxylic acid [32].

The process of creating a covalent attachment of PEG to another molecule, also known as *PEGylation*, can be reach in various ways.
In case of coupling a Carboxylic group $-COOH$ (the functional group X) with Nucleophiles (amine group in lysine residues or hydroxyl groups), for example, to achieve the formation of a covalent amide or ester bond, carbodiimide reagents are most commonly used [33]. Reagents such as dicyclohexyl carbodiimide (DCC) and 1-ethyl-3- (3-dimethylaminopropyl)carbodiimide (EDC) are examples of these reagents. The purpose of the carbodiimide reagent is to create a reactive O-acyl isourea intermediate with the carboxylic group, which is then reacted with a suitable nucleophile.

The coupling is normally performed in two steps, activation and reaction, in order to avoid reaction between the carbodiimide and the immobilized molecule. However, in acqueous solutions the reactivity of the intermediate is so high that water hydrolysis rapidly transforms it back to carboxilyc acid, if it is not trapped by another competing nucleophile. This side effect can be overcome using a mixture of carbodiimide and reactive hydroxyl compound, formin an active ester derivative that is stable for several minutes to hours. The hydroxyl compound used can be N-Hyfroxy succimide (NHS), for example, which has been found to be a very suitable reagent for these purposes and it is normally mixed at high concentrations with EDC in water. Both the EDC and NHS act as buffering agents and a pH around 5-6 is obtained, providing conditions for an optimal reaction rate for NHS ester formation. NHS is the usually preferred hydroxyl compound due to its solubility in water, low toxicity and optimal reactivity for two-stage couplings.

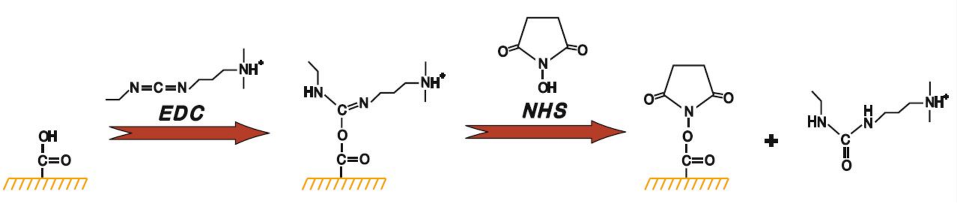

Figure 3.5: Representation of activation of the carboxylic acid group.

3.3 State of the Art: SPR Sensors for Food Safety

Illnesses can be transmitted through food. Foodborne desease are defined as “all those deseases evinced after the ingestion of food which contains pathogenic microorganisms or toxines” [34] whose main syntoms are usually gastrointestinal syntoms. These deseases represent a serious problem for the health of consumers and for the econonomy of companies and business services: some data, collected from province of Vicenza [34] (Veneto region) and from Emila-Romagna region [35] reveal that in 2009, in Italy, 248 centres of infections due to foodborne disease have been notified, involving about 1451 people. Only in Emilia-Romagna, during the period 1988-2010 1943 cases of foodborne diseases were reported, with the frequency expressed in Figure 3.6, with a total of 16889 ill people (and 52218 exposed people, people who shared the same meal) and 2702 hospitalized. Infections are mostly caused by bacteria; however, they are not the only form of contaminants of food. Proteins secreted from infectious bacteria, virus and mycotoxins can be other causes of foodborne desease.

The ability to identify contaminated food samples is of great importance to the food processing industry as well as to regulatory agencies. There is

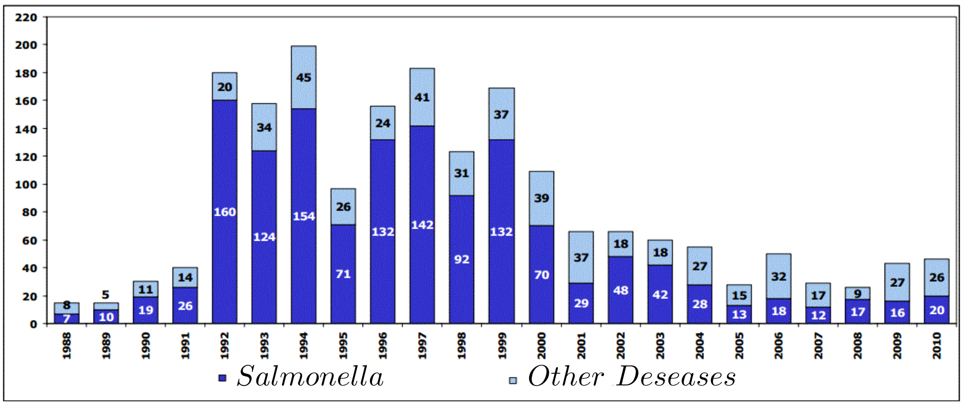

Figure 3.6: Episodes of foodborne diseases in Emilia-Romagna in each year from 1988 and 2010. Salmonella infection in dark blue, other infections in light blue [35].

a need for accurate techniques to rapidly detect the presence of foodborne pothogens; conventional techniques include culturing methods, polymerase chain reaction (PCR), flow cytometry and enzyme-linked immunosorbent assay (ELISA). However, all these techniques require highly specialized laboratory equipment and training; instead of these, surface plasmon resonance can be a portable, simple-to-use sensor which offers the advantage of performing real-time detections, making in-line monitoring of food processing possible. Hence, SPR sensors represent a good way to improve food safety.

In Emilia-Romagna, the etiological agents responsible for foodborne deseases during the period 1988-2010 are distribuited as represented in Figure 3.7 [35]. These agents and examples of SPR biosensor involved to dectect them are :

- **Salmonella spp.**, which is an infectious bacterium found in raw meat, poultry, seafood, eggs, milk and dairy products. The infective dose of Salmonella spp. can be as few as 15-20 cells, depending on the size and health of the individual.
  At first, in 2001, Koubová demonstrated detection of *Salmonella enteriditis* using a custom-built SPR system [36]. Antibodies were physisorbed onto a bare gold surface, leading to a detection of heat-killed and ehtanol soaked Salmonella enteritidis at a concentrations down to 10^6 cell/mL.
  Several reserches have been going on since that; in 2007 [37] Mazumdar and others demonstrated, using a SPR angular modulated sensor in Kretschmann configuration (*Plasmonic*® HS Systeme, Wellenfels, Germany), the detection of *Salmonella typhimurium* cells killed by thimerosal treatment in buffer and milk solution. In this case a SAM

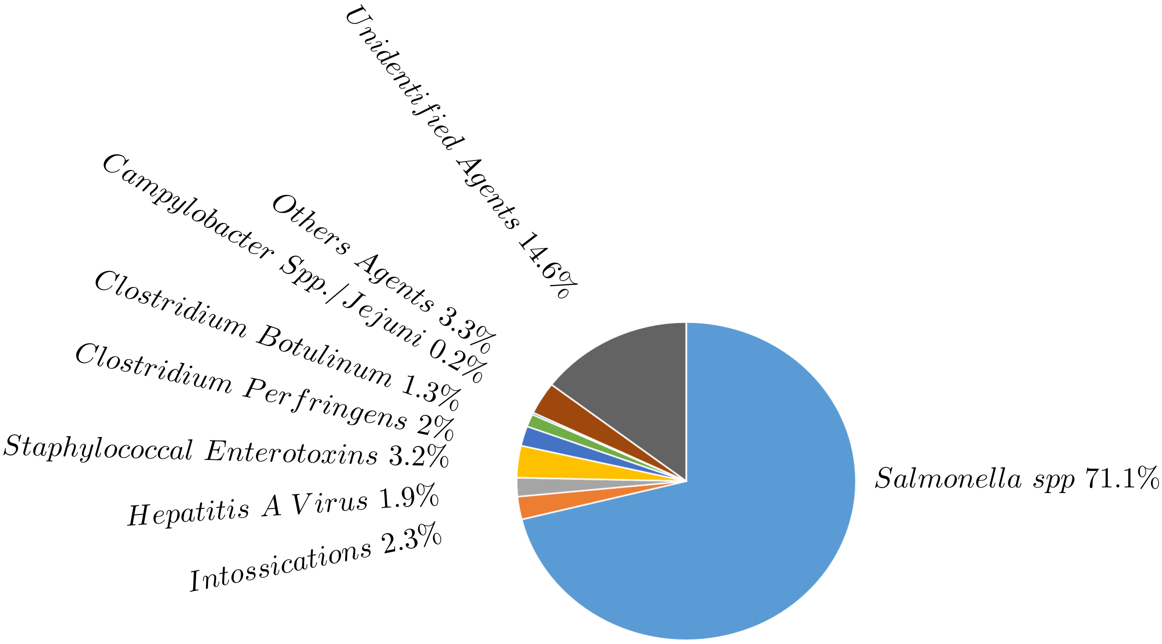

Figure 3.7: Agents responsible of food deseases in Emilia-Romagna during the period 1988-2010 [35].

layer of alkylsilane is grown on the gold surface (using a solution of C18-alkylsilane), preparing the surface for the immobilization of Polyclonal antibodies. The results, both in buffer and in milk, revealed a sensitivity comparable with commonly used and approved commercial *Salmonella* detection kit. The time required for the analysis was very low (1 hour), with the advantage of having real-time data of the binding events. Furthermore, the sample required for the analysis is only 10 μL.

- **Intossications** are due to various toxins (in general low molecular weight compounds) like algan toxis. One example of them is the domoic acid, a neuroexcitatory toxin tipically produced by planktonic algae. Found in Canadian, Portuguese, Spanish and Irish coast [38], the domoic acid contaminates shellfish (expecially mussels) whose ingestion by humans can cause an intoxication syndrome known as amnesic shellfish poisoning (ASP). ASP causes vomiting, cramps and temporary or permanent memory loss.
  In 2005 [39] a custom-buit SPR sensor based on Kretschmann configuration was created - DA was immobilized through NHS/EDC on a mixed SAM of oligo(ehylene glycol OEG) containing alkanethiols. DA was detected from a concentration of 0.1nG/mL, lower than that recognised by ELISA technique using the same antibody.

- **Staphylococcal Enterotoxins** are the most widely studied of the toxic foodborne proteins. This toxins are mainly produced by *Staphylococcus aureus* bacteria: there are nine enterotoxins (A, B, C, D, E, G, H, I, J) found in a wide variety of food like meat, poultry and egg products, milk and dairy products and bakery products.
  Nedelkov demonstrated the detection of staphylococcal enterotoxin B in 2000 [40]: he used samples of milk and mushroom cointaining 100, 10 and 1 ng/mL of staphylococcal enterotoxin B (SEB) and observed a consistent change of reflectance value.
  In 2009 [41], Tsai developed an SPR immunosensor based on angular modulation for determining staphhylococcal enterotoxin A. He used a gold surface functionalized with SAM layer - using thiols with carboxyl (16-MHA) and hydroxyl (6-MCH) terminal groups. The carboxylic groups of the mixed SAMs were activate with a mixture of EDC/NHS, leading to the bond of anti-SEA (*Staphylococcal Enterotoxins A*). Even if with this sensor he was able to recognise concentrations of SEA in the range of 100-1000ng/mL, lower concentrations can cause intoxication as well. Hence, sensitivity still needs to be enhanced to prevent food poisoning.

- **Clostridium Perfringens**, bacterium found in soil, sediments and areas subjected to human or animal fecal pollution. Food poisoning is caused by ingestion of toxin-producing *C. Perfringens* bacteria - poisoning confirmed by detecting the toxin in the feces of patients. The β-toxin produced by *Clostridium Perfringens* was detected thorugh SPR in 1998 by Hsieh [42]. He compared the results obtained by SPR method with enzyme-linked immunosorbent assay, observing a comparable resolution but with a reduced time requested.

- **Clostridium Botulinum**, which produces Botulinum neurotoxins (seven serotypes, A, B, C, D, E, F and G). Two of them, C and D, are found in birds and non-human mammals, while A, B, E and F have been implicated in human cases of botulism. Those neurotoxines have been found in a lot of food, including honey, vegetables pickled in oil and chili.
  An example of SPR sensor employed in detection of Botulinum was realized by Ladd and others in 2008 [43]. He used a SPR custom biosensor in Kretschmann configuration to detect toxines A, B and F in buffer and in 20% honey solution. To fix the antibody to the gold surface, a OEG (oligo ethylene glycol) alkanethiol was used, creating a SAM. A wavelength modulation SPR sensors was used to detect different toxin concentration, from 0.5 to 10 ng/mL, obtaining results comparable between buffer and honey solution.

- **Campylobacter Jejuni**, is a bacterium carried by healthy cattle, chickens and non-chlorinated water sources. The infective dose is quite small because it's considered that only 400-500 bacteria might cause illness. An example of development of a SPR biosensor to detect Campylobacter Jejuni can be found in literature thanking to Wei and Simonian in 2007 [44]. Wei and Simonian used two channel SPR angular modulation sensor (*Spreeta*®, Texas Instruments, Dallas, TX) with Kretschmann's geometry to detect C.J. in pure culture and broiler meat rinse spiked with the bacterium.

3.4 Measurement Set-up

The $LUXOR$ ($Laboratory\ for\ Ultraviolet\ and\ X-ray\ Optical\ Research$) Kretschmann bench of CNR-INF Institute of Padova used for all collected data in This thesis is a SPR sensor based on prism coupling. It consists of the following instruments:

- a THORLabs He-Ne laser system (Figure 3.8), with the following characteristics:
    - $\lambda = 633$ nm;
    - $P = 5$ mW;
    - Beam diameter (TEM_{00}) $0,81$ mm;
    - Beam divergence 1 mrad;
    - Longitudinal Mode Spacing 435 MHz;
    - Max noise (RMS, 30 Hz to 10 MHz) 0.2%;
    - Operating current 6.0 ± 0.1 mA.

Figure 3.8: CAD image of the Laser source

- lens polarizator which is used to create a p-polarized light.

Figure 3.9: CAD image of Photodetector

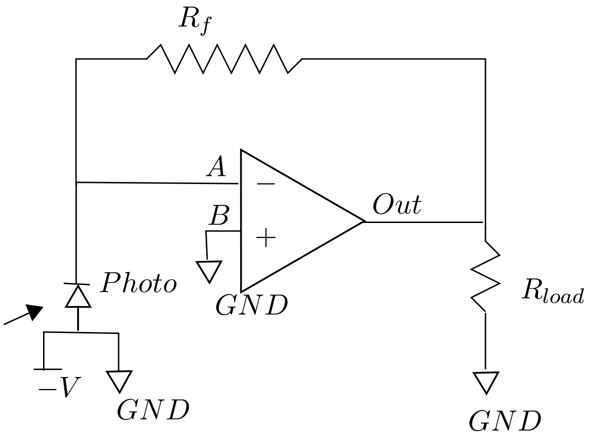

Figure 3.10: Scheme of the photodetector

- a THORLabs PDA-100A-EC photodetector (Figure 3.9), whose operation theory can be schematized as in Figure 3.10. It consists in a photodiode connected to a transimpedance Amplifier.

  Its features are:

  - *Responsivity* which is the ratio of generated photocurrent to the incident power at a given wavelength

    $$R(\lambda) = \frac{I_{PD}}{P} = 0.62\,\frac{A}{W}(Typ) \tag{3.14}$$

    where I_{PD} is the photocurrent and P is the incident light power.

  - *Dark current* which is leakage current which flows when a bias voltage is applied to a photodiode. Thanking to the transimpedance amplifier, the dark current flowing out can be well-controlled;

  - the bandwith of the sensor can be calculate by the following formula:

    $$f_{-3dB} = \sqrt{\frac{GBP}{4\pi R_f \times C_D}} \tag{3.15}$$

    where $GBP = 600$ MHz is the amplifier gain bandwidth product, C_D is the sum of the photodiode junction capacitance and the amplifier capacitance, R_f is the feedback element. This value is strictly dependent on the gain setting applied; hence, in the configuration used for all the acquisition of data (Gain= 40 db setting), $f_{-3dB} = 225$ kHz;
  - the noise of 799 μV RMS for 40 dB setting;
  - the terminating resistance modifies the voltage value by the factor

    $$Scale = \frac{R_{load}}{R_{load} + R_s} = \frac{R_{load}}{R_{load} + 50} \tag{3.16}$$

    leading to the following output:

    $$V_{out} = R(\lambda) g_m Scale P = 0.62 \times g_m \times Scale \times P; \tag{3.17}$$
  - an active area of 100 mm^2;
  - a wavelength range from 340 to 1100 nm;
  - an output voltage from $0V$ to $5V$ (considering $R_{load} = 50\ \Omega$).

- another photodiode array for position identification.
  Because the socket (cointeinment structure for the prism) allows a little rotating movement, there is the possibility that the prism surface is not exactly normal to the laser light beam when beginning the measurement. For this reason there is an offset error due to the initial position of the prism, different everytime the bench is prepared. The reflected light can be useful to settle the zero - it is known that the surface of the prism is normal to the laser ray when the reflected ray superimposes the incoming light. Hence, knowing that the reflected ray passes through the position photodiode (Figure 3.11) when

  $$\theta = \arctan\left(\frac{d}{L}\right) \approx \arctan\left(\frac{1.08cm}{100cm}\right) \approx 0.62^o \tag{3.18}$$

  it is possible to use the data acquired by the position photodiode array to have a reference value with which to move data acquired by the photodetector.
  The photodiode array used is Hamamatsu S4111; its features are:

  - an active area for each element of $1.45 \times 0.9\ mm^2$ (effective active area 1.305 mm^2);

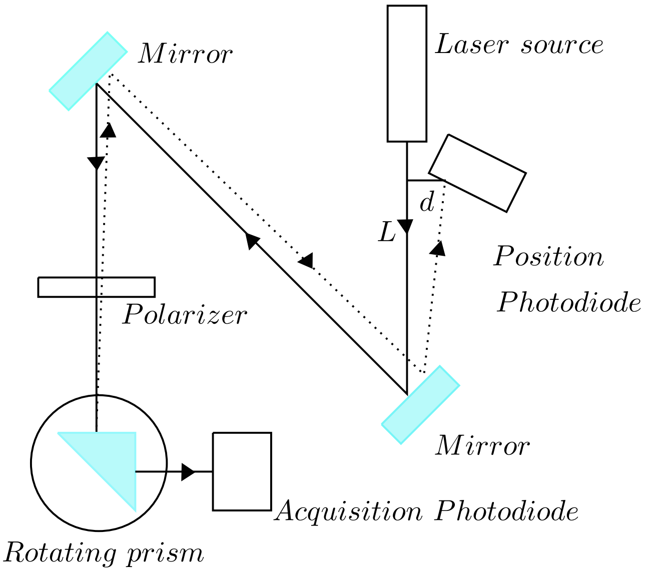

Figure 3.11: Scheme of the bench - reflected ray a position photodiode

- a maximum reverse voltage $V_R = 15$ V;
- a spectral response range from $\lambda = 340$ nm to 1100 nm;
- a peak sensitivity wavelength $\lambda_p = 960$ nm;
- a photo sensitivity at $\lambda = 633$ nm of $S = 0.39\ \frac{A}{W}$;
- a maximum dark current from 5 to 25 pA (respectively for $V_R = 10\ mV$ and $V_R = 10\ V$);
- a typical shunt resistance at 10 mV of 250 $G\Omega$;
- a terminal capacitance C_t between 200 and 50 pF.

In Figure 3.12 is represented the operation circuit scheme.

- a motor device, connected with Labview Software.
  The Labview software, designed at Biodevice Lab., acquires data from photodiode through a step-by-step acquisition: at first the motor device supporting the prism reaches the desired angle; then the motor supporting the photodiode reaches the desired angle as well (the motor angle needs to be equal to the photodiode angle for the Snell's law)

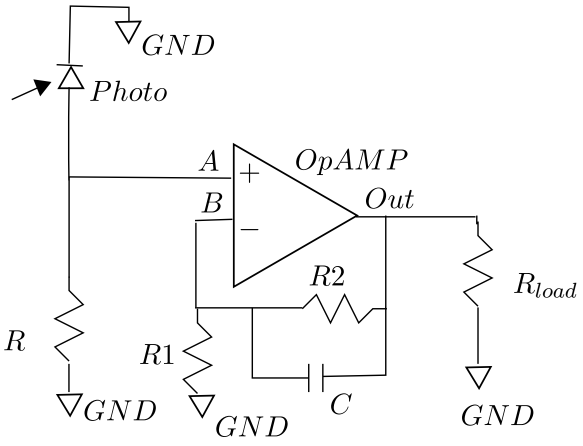

Figure 3.12: Scheme of the photodiode array

and only after those steps there is the data aquisition, which corresponds to 1000 data samples collected (1000 data for each acquisition, data wich are averaged). However, because this step by step procedure requires two movements of motors for each acquisition, a lot of time is needed to perform a full range low step analysis. Hence, to reduce this scanning time, during the acquisition of data (as explained in Protocols, chapter 4 section 1), a reasonable high acquisition step is used (normally 0.05^o of motor angle) and data are fitted by MATLAB software, as explained in chapter 4 section 1.

The functionment of the acquisition software can be schematized as in Figure 3.13.

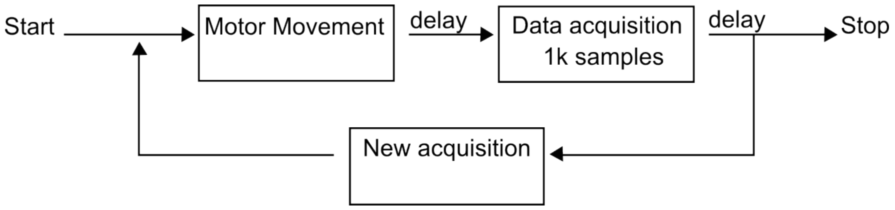

Figure 3.13: Scheme of the acquisition LabView Software

- a socket (containment structure for the prism and the device), designed appositely for the Kretschmann bench.

In a classical angular scanning system for a prism coupler, in which

the rotation axis passes through the diagonal of the prism, when the motor rotates there is a change of the prism incident angle θ_i. This modification of the incident angle causes a movement of the light spot on the metallic surface so that the point of the metal hit by the laser is not always the same during a measurement.
In order to reduce this movement on the metallic surface, i.e., to measure the smallest area, a socket has been designed. It consists of a contaiment structure of plastic which is used to modify the position of the prism on the motor, changing so the position of the rotation axis into the prism.

To develop this socket, only the *Snell's law* and the prism geometry are used [45].

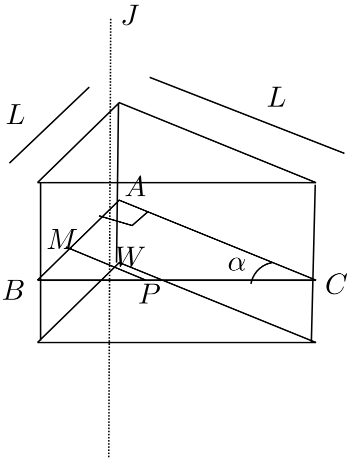

Figure 3.14: Scheme of the prism

Considering Figure 3.14, ABC is the cross section of the isoceles prism $AB = AC = L$ and α is the base angle. Point P is on BC and point M is on AB. MP is perpendicular to AB. J considered as the rotation axis, goes vertically through the cross section ABC of the prism at point W, called rotation centre.
The geometric method is used to determine the optimal position of the rotation axis: if P is a light source, its light rays can enter the air through glass medium. For the reversibility principle of the light, refractive rays (new sources) will converge at the point P if the refractive rays propagate back. If the refractive rays are extended and intersect at one point, it is possible to set this point as the rotation centre W. However, those rays cannot intersect in one single point: they can draw a dense area of intersection points. In this case, setting one of the points in this area as W, all the light rays produced from the rotation of the prism go near the position P, minimizing in this way

the previous discussed *movement* on the metallic surface. Of course, it needs to be remebered that W should be put on the normal to AB for simmetry.

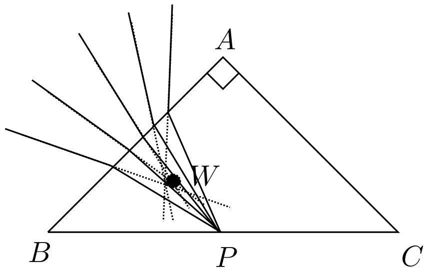

Figure 3.15: Setting of W

In the case of Kretschmann bench, the prism considered is an isosceles triangle prism (with the angle $B\hat{A}C = 90^o$), $n_p = 1.47$ and $n_{poly} = 1.586$. Considering the Figure 3.16, when the light comes out of the point E, by applying the *Snell's law* and remembering that $\theta_3 = \theta_2 - 45^o$ it is possible to obtain the position of H and the angle θ_4 knowing the position of E and θ_1.

$$E = \left[\frac{a+d}{\sqrt{2}}, L + \frac{d-a}{\sqrt{2}}\right]$$

$$F = \left[\frac{a}{\sqrt{2}}, L - \frac{a}{\sqrt{2}}\right]$$

$$G = \left[X_F + \frac{d\tan\theta_1}{\sqrt{2}}, Y_F - \frac{d\tan\theta_1}{\sqrt{2}}\right]$$

$$H = [X_G + Y_G \tan\theta_3, 0] \tag{3.19}$$

$$\theta_2 = \arcsin\left(\sin\theta_1 \frac{n_{poly}}{n_p}\right)$$

$$\theta_3 = \theta_2 - 45$$

$$\theta_4 = \arcsin\left(\sin\theta_3 \frac{n_p}{n_{air}}\right) \tag{3.20}$$

Once the position H and the angle θ_4 has been found, we consider the rotation centre W as the intersection between the perpendicular to the AC line and the extension of rifracted ray. Then, it is possible to find the position of E as a function of the angle θ_4:

$$H = [W_x + W_y \tan\theta_4, 0]$$

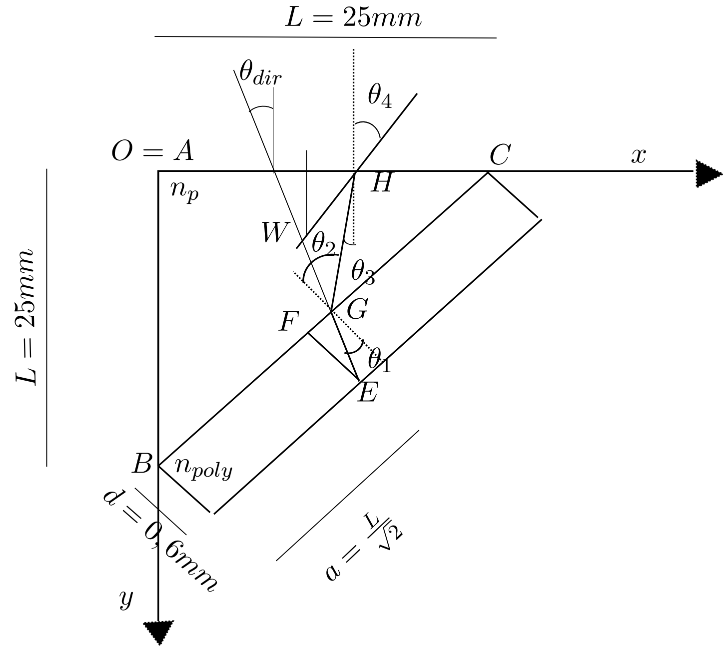

Figure 3.16: Scheme used for calculation of W

If we calculate the line passing through G and H it's possible to calculate the position of G

$$m_1 = -\frac{\cos\theta_3}{\sin\theta_3} \qquad q_1 = -m_1 H_x$$

$$G = \left[\frac{L-q_1}{m_1+1}, -\frac{L-q_1}{m_1+1} + L\right]$$

Calculating the line passing through G and E (so obtaining m_2 and q_2 it's possible to get E:

$$m_2 = \frac{\cos\theta_{dir}}{\sin\theta_{dir}} \qquad q_2 = G_y - m_2 G_x$$

$$E = \left[\frac{L+d\sqrt{2}-q_2}{m_2+1}, -\frac{L+d\sqrt{2}-q_2}{m_2+1} + L + d\sqrt{2}\right] \tag{3.21}$$

$$\theta_3 = \arcsin\left(\sin\theta_4 \frac{n_{air}}{n_p}\right)$$

$$\theta_2 = \theta_3 + 45^o$$

$$\theta_1 = \arcsin\left(\sin\theta_2 \frac{n_p}{n_{poly}}\right)$$

$$\theta_{dir} = 45^o - \theta_1$$

E is the point in which light rays hit the metal with this new rotating axis. Now, E depends on θ_{dir} (or θ_4) and on the position of W. Finding the coordinate for W is an optimization problem, which can be solved by differentiation for example.
To solve it by differentiation, it is necessary to minimize the distance between E and $\left[\frac{a+d}{\sqrt{2}}, L + \frac{d-a}{\sqrt{2}}\right]$ finding the best value for W_x and W_y; hence to minimize

$$f(W_x, W_y, \theta_{dir}) = \sqrt{\left(E_x - \left(\frac{a+d}{\sqrt{2}}\right)\right)^2 + \left(E_y - \left(L + \frac{d-a}{\sqrt{2}}\right)\right)^2} \tag{3.22}$$

considering θ_{dir} as a parameter.
It can be solved by writing a MATLAB code. Results obtained are $[W_x, W_y] = [13.8; 7.5]$: in Figure 3.17 are reported the values of the distance between E and $\left[\frac{a+d}{\sqrt{2}}, L + \frac{d-a}{\sqrt{2}}\right]$ as a function of W_x and W_y position.

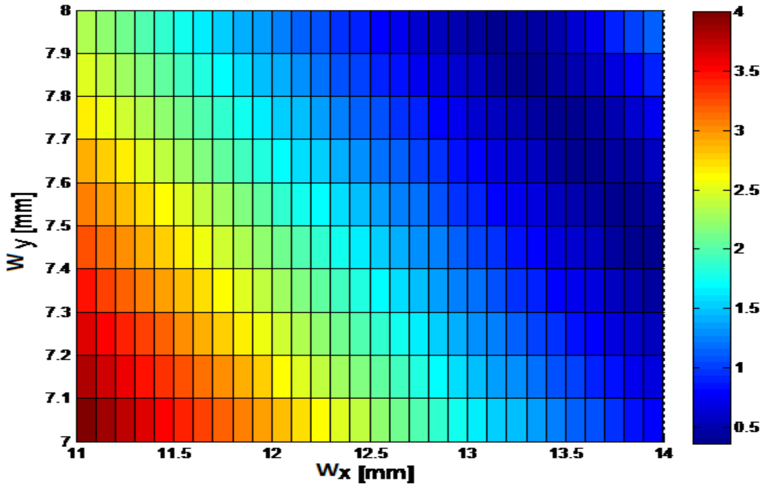

Figure 3.17: Value of distance between E and $\left[\frac{a+d}{\sqrt{2}}, L + \frac{d-a}{\sqrt{2}}\right]$ as a function of W_x and W_y.

To demostrate experimentally the difference between using/not using the socket, we can use graph paper fixed on the metal to follow the laser spot on the device surface - hence, we “visually” calculate the movement of the spot laser on it.
By performing an angular scanning (from -30^o to $+30^o$ with a step of 5^o), it is possible to set the point position of the laser spot at each angular position. The results are plotted in Figure 3.18.

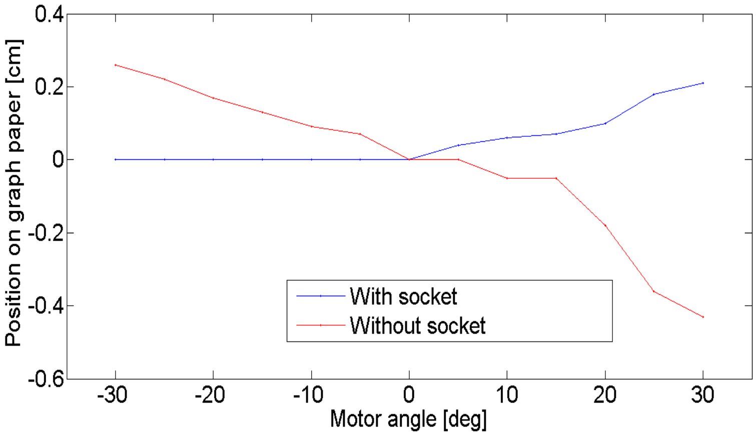

Figure 3.18: Position of laser spot on graph paper. Red curve with the classical configuration (without socket, rotating axis passing through the prism diagonal), blue curve with socket (rotating axis inside the prism).

From Figure 3.18, it's possible to see that the movement of the spot on the graph paper is definitely reduced using the socket. In case of using the socket, the total movement of the spot is about 2 mm; in case of the classical configuration, it is about 6.9 mm.
From this simple experiment, we can infer that the socket structure works correctly: it reduces the area hit by the laser while performing an angular motor scanning.

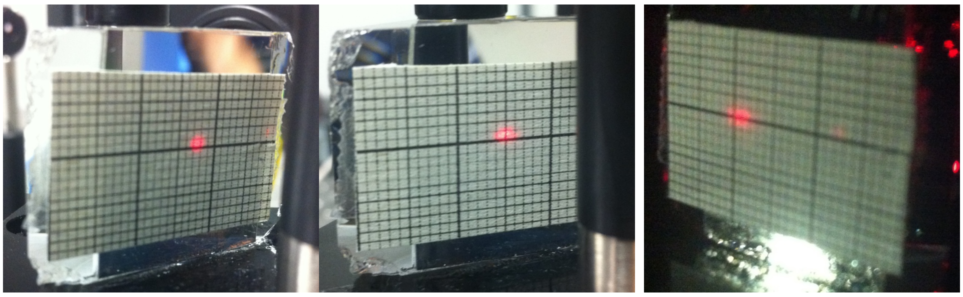

(a) -30^o (b) 0^o (c) 30^o

Figure 3.19: Laser spot position in classical configuration

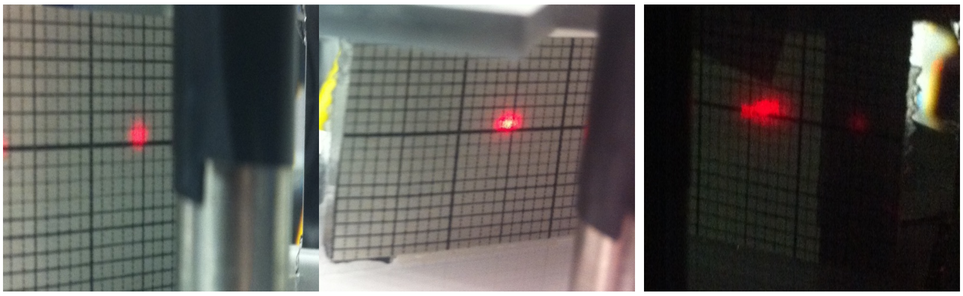

(a) -30^o (b) 0^o (c) 30^o

Figure 3.20: Laser spot position with socket

3.5 Simulation of a Multilayer System

When in Chapter 1 the Prism Coupling theory has been explained, a new structure composed by three materials (prism, metal, dielectric) has been proposed. However, this three layers structure is quite different from the theoretical two-infinite media discussed. Hence, the question that comes out is the following one: - how does the third layer change the theoretical behaviour?

The answer comes out from this simulated analysis based on matrix method for multible beam interference. The method and the derivation proposed is based on the work made by Klein and Furtak [46].

The MATLAB program based on matrix method is also used to predict the behaviour of the experimental bench.

The simulation describes the behaviour of a device composed by prism, metal and dielectric in terms of reflectivity and trasmittivity. To achieve these two expressions four steps are required:

1. the refracted and reflected parts of an incident wave is expressed as a function of the incoming wave;

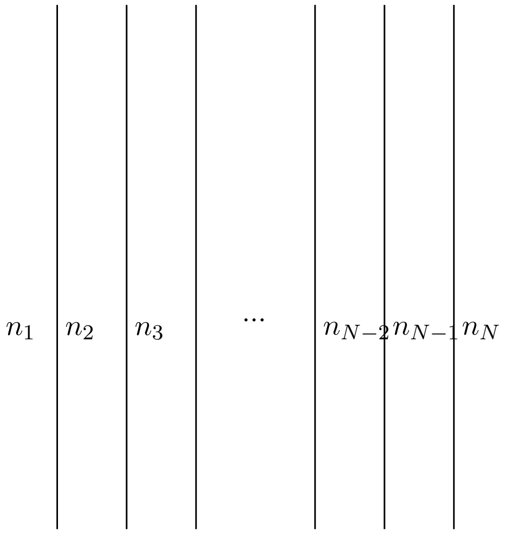

Figure 3.21: Multilayers structure

2. the equations obtained in the first step are combined to a matrix set-up, in which each matrix describes the behaviour at an interface;
3. other matrices describe the behaviour of the light while passing through layers;
4. all matrices are combined to obtain one single matrix which describes multiple stacked media.

Now it is considered a single interface between two media, i and j, with refractive index n_i and n_j (they can be complex numbers).

- E_{t_i} is the electric field of the light travelling from medium i to medium j in medium i.
- E_{t_j} is the electric field of the light trasmitted through the interface travelling from medium i to medium j in medium j.
- E_{r_i} is the electric field of the light reflected by the interface, travelling from medium j to medium i in medium i.
- E_{r_j} is the electric field of the light travelling from medium j to medium i in medium j.

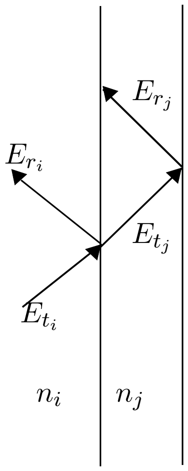

Figure 3.22: Interface between two media and electric fields of light

Remembering the definitions of the reflection coefficients

$$\rho_{ij} = \frac{E_{r_i}}{E_{t_i}} \qquad \rho_{ji} = \frac{E_{t_j}}{E_{r_j}} \qquad \tau_{ij} = \frac{E_{t_j}}{E_{t_i}} \qquad \tau_{ji} = \frac{E_{t_i}}{E_{t_j}}$$

it is possible to write

$$E_{t_j} = \tau_{ij} E_{t_i} + \rho_{ji} E_{r_j} \tag{3.23}$$

If the incident EM wave is p-polarized (TM), which means that E field is in the plane of incidence, τ_{ij} and ρ_{ji} are given by:

$$\tau_{ij} = \frac{2n_i}{(1+b)n_j} \tag{3.24}$$

$$\rho_{ij} = \frac{1-b}{1+b} \tag{3.25}$$

where the term b is

$$b = \left(\frac{n_i}{n_j}\right)^2 \left(\frac{k_{z_j}}{k_{z_i}}\right) \tag{3.26}$$

and k_{z_i} and k_{z_j} are respectively the projection of the wavevector k to the z-axis in medium i and j. Another expression can be created, like that in equation (3.23)

$$E_{r_i} = \rho_{ij} E_{t_i} + \tau_{ji} E_{r_j} \tag{3.27}$$

By combining (3.23) and (3.27) E_{t_i} can be eliminated, leading to

$$E_{r_i} = \left(\frac{\tau_{ji}\tau_{ij} - \rho_{ji}\rho_{ij}}{\tau_{ij}} \right) E_{r_j} + \frac{\rho_{ij}}{\tau_{ij}} E_{t_j} \tag{3.28}$$

This equation can be further reduced by remembering that

$$\rho_{ij} = \frac{1-b}{1+b} = \frac{n_j^2 k_{z_i} - n_i^2 k_{z_j}}{n_j^2 k_{z_i} + n_i^2 k_{z_j}} = -\frac{n_i^2 k_{z_j} - n_j^2 k_{z_i}}{n_j^2 k_{z_i} + n_i^2 k_{z_j}} = -\frac{1-\frac{1}{b}}{1+\frac{1}{b}} = -\rho_{ji}$$

$$\tau_{ij}\tau_{ji} + (\rho_{ij})^2 = \frac{4}{(1+b)(1+\frac{1}{b})} + \frac{(1-b)^2}{(1+b)^2} =$$

$$= \frac{4}{2+\frac{1}{b}+b} + \frac{(1+b)^2-4b}{(1+b)^2} = \frac{4b}{(b+1)^2} + 1 - \frac{4b}{(1+b)^2} = 1$$

obtaining

$$E_{r_i} = \left(\frac{1}{\tau_{ij}} \right) E_{r_j} + \left(\frac{\rho_{ij}}{\tau_{ij}} \right) E_{t_j} \tag{3.29}$$

and, by applying the same procedure on (3.23) equation, another expression is obtained

$$E_{t_i} = \left(\frac{\rho_{ij}}{\tau_{ij}} \right) E_{r_j} + \left(\frac{1}{\tau_{ij}} \right) E_{t_j} \tag{3.30}$$

These two equations can be organized in a matrix structure:

$$\begin{pmatrix} E_{r_i} \\ E_{t_i} \end{pmatrix} = \frac{1}{\tau_{ij}} \begin{pmatrix} 1 & \rho_{ij} \\ \rho_{ij} & 1 \end{pmatrix} \begin{pmatrix} E_{r_j} \\ E_{t_j} \end{pmatrix} \tag{3.31}$$

which is

$$\mathbf{E}_i = \mathbf{H}_{ij}\mathbf{E}_j \tag{3.32}$$

where $\mathbf{H}_{ij}$ is the matrix which describes the fields transition thorugh the interface of the two media.

When the light is travelling through a medium, its general expression is $E = E_0 e^{j\mathbf{k}\cdot\mathbf{r}} e^{-j\omega t}$. When a matrix for a certain interface is calculated, it is created respectively to its own coordinate system, with the origin set on the interface. However, when working with more than one interface, a common coordinate system must be found. For this reason the coordinate system is chosen on the first interface, while every other interface is referred to the previous one by a change in phase

$$E_i = E_0 e^{j\mathbf{k}\cdot(\mathbf{r}+\mathbf{d}_i)} e^{-j\omega t}$$

where $\mathbf{d}_i$ is the thickness of the i-layer. Because $\mathbf{d}_i$ is a vector parallell to z-axis

$$j\mathbf{k}\cdot\mathbf{d}_i = jk_{z_i}(d_i) = jk_0 n_i \cos(\theta_i) d_i$$

it leads to

$$\begin{aligned} E_{r_j}(z=d_j) &= E_0 e^{j(k_{x_j}x+k_{z_i}d_j)}e^{-j\omega t} = \\ &= E_0 e^{jk_{x_j}x}e^{-j\omega t}e^{jk_{z_j}d_j} = e^{jk_{z_j}d_j}E_{r_j}(z=0) \qquad (3.33) \\ E_{t_j}(z=d_j) &= E_0 e^{j(k_{x_j}x-k_{z_j}d_j)}e^{-j\omega t} = \\ &= E_0 e^{jk_{x_j}x}e^{-j\omega t}e^{-jk_{z_j}} = e^{-jk_{z_j}d_j}E_{t_j}(z=0) \qquad (3.34) \end{aligned}$$

where the origin of the coordinate system is set on the ij-interface. Rewriting in a matrix form

$$\begin{pmatrix} E_{r_j}(z=d_j) \\ E_{t_j}(z=d_j) \end{pmatrix} = \begin{pmatrix} e^{jk_{z_j}} & 0 \\ 0 & e^{-jk_{z_j}} \end{pmatrix} \begin{pmatrix} E_{r_j}(z=0) \\ E_{t_j}(z=0) \end{pmatrix} \qquad (3.35)$$

Thus, inverting the matrix it's possible to obtain the relation between $E_j(z=0)$ and $E_j(z=d_j)$

$$\begin{pmatrix} E_{r_j}(z=0) \\ E_{t_j}(z=0) \end{pmatrix} = \begin{pmatrix} e^{-jk_{z_j}} & 0 \\ 0 & e^{jk_{z_j}} \end{pmatrix} \begin{pmatrix} E_{r_j}(z=d_j) \\ E_{t_j}(z=d_j) \end{pmatrix} \qquad (3.36)$$

This 2x2 matrix is called *propagation matrix* $\mathbf{L}_j$

By combining **H** and **L** matrices of several layers it's possible to obtain a total matrix for a stack of N layers

$$\mathbf{H}_{12}\mathbf{L}_2\mathbf{H}_{23}\mathbf{L}_3 \cdot \mathbf{H}_{ij}\mathbf{L}_j \cdot \mathbf{H}_{(N-1)N} = \begin{pmatrix} S_{11} & S_{12} \\ S_{21} & S_{22} \end{pmatrix} \qquad (3.37)$$

which corresponds to

$$E_{r_1} = S_{11}E_{r_N} + S_{12}E_{t_N}$$

$$E_{t_1} = S_{21}E_{r_N} + S_{22}E_{t_N}$$

We can define the *reflection coefficient* of the stack ρ and the *transmission coefficient* τ in relation with the obtained parameters

$$\rho = \left.\frac{E_{r_1}}{E_{t_1}}\right|_{E_{r_N}=0} = \frac{S_{12}}{S_{22}} \qquad \tau = \left.\frac{E_{t_N}}{E_{t_1}}\right|_{E_{r_N}=0} = \frac{1}{S_{22}} \qquad (3.38)$$

Reflectance and *Transmittance* can be obtained from ρ and τ by the following relations

$$R = \frac{P_r}{P_i} = |\rho|^2 \qquad T = \frac{P_t}{P_i} = |\tau|^2 \frac{n_N \cos(\theta_N)}{n_1 \cos(\theta_1)} \qquad (3.39)$$

where P_i is the power of the incident wave, P_r is the power of the reflected wave, P_t is the power of the transmitted wave, θ_1 is the angle of the incident light and θ_N is the angle of the transmitted wave.

The same analysis can be performed with a TE polarized light. However, in case of s-polarization, some values must be modified:

$$\tau_{ij} = \frac{2}{1+b} \tag{3.40}$$

$$\rho_{ij} = \frac{1-b}{1+b} \tag{3.41}$$

where the term b is

$$b = \frac{k_{z_j}}{k_{z_i}} \tag{3.42}$$

The other relations (i.e. $\rho_{ij} = -\rho_{ji}$) are still valid.

Chapter 4

Experimental Results

The experimental results described in this Chapter belongs to a research activity of the BioDevices Laboratory of the Department of Information Engineering. The project's aim is to develop a SPR sensor able to recognize biological molecules (like bacteria, proteins and toxins) in wines. This Chapter describes the opto-electrical characterization of:

- bare silver devices;
- silver devices with a PEG SAM;
- silver devices with detection sandwich, i.e., PEG SAM conjugated with probe antibodies.

In this Chapter, all adopted protocols for collecting data are presented. These include:

- *cleaning protocol*, which corresponds to the methodology used to clean devices involved in measurement;
- *fuctionalization protocol*, which corresponds to the methodology used to cover the metallic surface with a biomaterial layer;
- *immobilization of antibody protocol*, which corresponds to the methodology used to activate the functional group at the end of PEG and to bond the antibodies;
- *measurement protocol*, which corresponds to the methodology used to collect data - hence all the operations performed when acquiring data;
- *data analysis*, which corresponds to the way data are analyzed.

Then, all results are compared to simulated results predicted by MATLAB simulation software described in Chapter 3.

4.1 Devices

For these experimental results, two kind of devices are employed:

- a *flat device* of O.D. 1500, consisting in a substrate of polycarbonate ($n = 1.586$) which supports a thin layer of silver (thickness of 40 nm). The substrate has been produced via policarbonate molding onto which the silver layer has been evaporated.
  In Figure 4.1 the section of the device is represented. A photo of the device is in Figure 4.2;

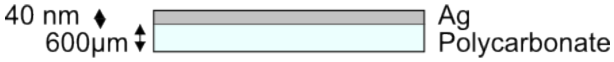

Figure 4.1: Section of flat device of O.D. 1500

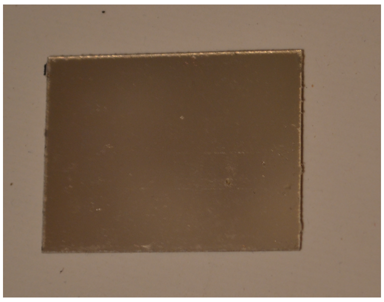

Figure 4.2: Photo of the flat device

- *grating device* of O.D. 2500, consisting in a silver nanostructure $50-60$ nm thick with period $\Lambda \approx 740$ nm evaporated onto a policarbonate layer. The section of the device is represented in Figure 4.3; a SEM image aquired at Padova University and an AFM image are then reported in Figure 4.4.

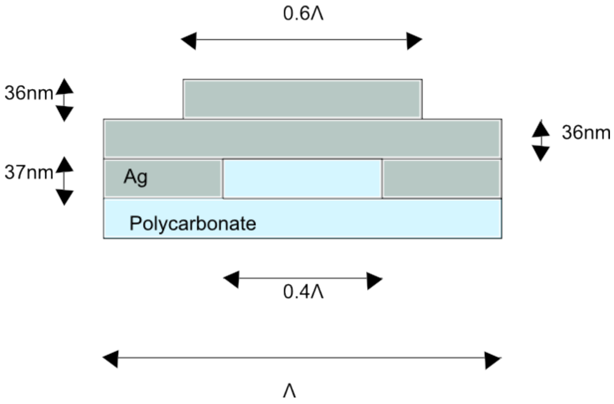

Figure 4.3: Section of grating device

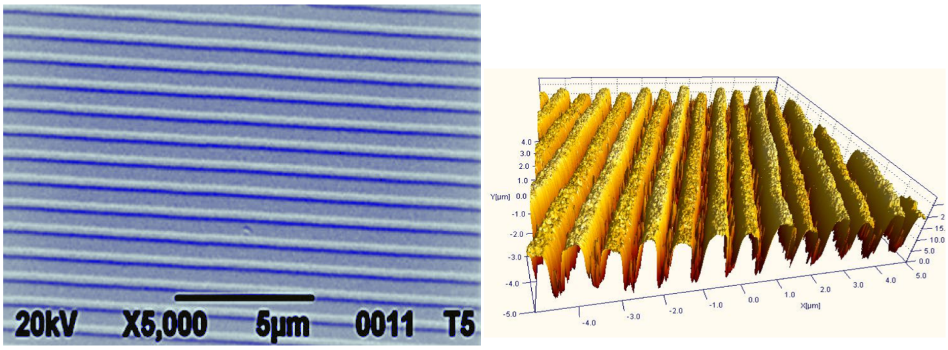

(a) SEM picture (b) AFM picture

Figure 4.4: Images of a grating device provided by Next Step Engineering s.r.l..

All devices have been provided by Next Step Engineering s.r.l..

4.2 Protocols

When performing a measurement, the appropriate sequence of operations has to be adopted in order to ensure repeatability. Protocols involving biological material have been carried out at Veneto Nanotech facilities. The protocols used for the measurements are:

- the *Cleaning Protocol*, which is organized as follows:
    1. the device is rinsed with absolute ethanol on the metal and on the polycarbonate surface;
    2. the device, still wet of ethanol, is rinsed with milli-Q water i.e. ultrapure water obtained by purification processes involving steps of filtration and deionization;
    3. the wet device is dried with compressed air.
- the *measurement protocol*, which is defined as follows:
    1. the preparation of the optical bench: the coupling between the prism and the polycarbonate layer is obtained by ceddar wood oil “Cargille - Type A”;
    2. the prism/device is placed on the sideburn, after fixing the socket;
    3. allineation of the reflected laser beam with the incident laser beam (hence setting the angular offset to zero by visual analysis);

4. angular scanning of the device: this is obtained moving the motor using the LABview software. Two different kinds of angular scanning have been used:
    (a) the range of -1^o to $+1.5^o$ of the motor angle with an acquisition step of 0.05^o in case of prism with refractive index of $n = 1,47$;
    (b) the range of -4^o to 1^o of the motor angle with an acquisition step of 0.05^o in case of prism with refractive index $n = 1.51$.

- the *PEG functionalization protocol*, which is organized as follows:

1. PEG is a pre-weighted powder situated in a plastic test tube *Eppendorf*. To prepare the solution of PEG, the following formula is used:

$$Molarity[M] = \frac{mass[g]}{AtomicWeight[Da] \times Solvent[l]} \tag{4.1}$$

from which, inverting it,

$$Solvent[l] = \frac{mass[g]}{AtomicWeight[Da] \times Molarity[M]} \tag{4.2}$$

The solution is prepared using milli-Q water, using appositely Single Channel Pipettes, able to measure the solution with high precision. The milli-Q water is added directly in the *Eppendorf*;

2. the device is placed on a plastic mask with $3.5 \times 3.5\ mm^2$ wells (see Figure 4.5), whose aim is to create a limited area of the metal which is in contact with the solution;

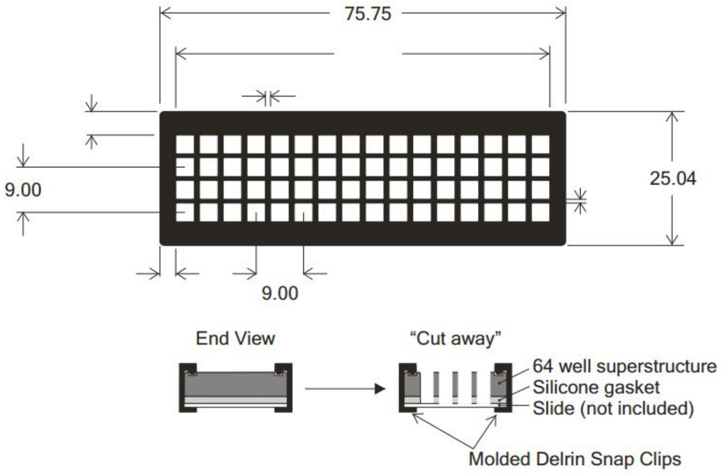

Figure 4.5: 64-Well ProPlate Slide Module Foorprint: the mask used for PEG and antibody immobilization

3. wells of the plastic mask are filled with 30 μl of PEG (or 30 μl of milli-Q if that area needs to be kept in a bare condition), following a pre-determined scheme;
4. the mask is enclosed into a Petri dish with cotton soaked with NaCl solution. The box is used to control the humidity of the space in order to avoid the drying of the solution;
5. the devices and the mask are kept inside the box for about 10/15 hours (one night);
6. the devices are removed from the plastic mask;
7. the devices are rinsed with milli-Q water;
8. the devices are dried with compressed air.

- the *diluition protocol*, which is used when it is necessary to decrease the concentration of a solute in solution by mixing with more solvent. This protocol is applied when PEG solution at a certain (lower) concentration is needed from a already prepeared solution of PEG. It is organized as follows:

  1. by knowing the volume of the solution to use ($Vol_{solution}$) and the concentrations it is possible to calculate the volume of solvent $Vol_{solvent}$ to add following the formula:

  $$Conc_{solution}[M] \times Vol_{solution}[l] =$$

  $$= Con_{diluited}[M] \times (Vol_{solution}[l] + Vol_{solvent}[l]) \tag{4.3}$$

     which, rearranged

  $$Vol_{solvent}[l] = \frac{Conc_{solution}[M] \times Vol_{solution}[l]}{Con_{diluited}[M]} - Vol_{solution}[l] \tag{4.4}$$

     gives the exact quantity of solvent (milliQ in our case) to add to the pre-existent solution;
  2. the right volume of the solution to use is obtained by using Single Channel Pipettes: this volume is placed in the *Eppendorf*;
  3. the right volume of the solvent (milliQ) to use is obtained by using Single Channel Pipettes: this volume is placed in the *Eppendorf*;
  4. the solution is mixed by shaking the *Eppendorf*;
  5. the solution is placed in the wells of the mask following a pre-determined scheme.

- *Immobilization of antibody protocol*: this protocol is used to activate and immobilize anti-Escherichia Coli polyclonal antibodies of rats on the PEG coated surface. It consists in the following steps:

1. a solution 5 mM of EDC and 5 mM of s-NHS in MES buffer 1X pH 6 (composed by 0.1 M MES (2-[morpholino]ethanesulfonic acid, 0.5 M NaCl pH 6) is prepared;
2. the solution is placed on the PEG surface and kept there for 15 minutes;
3. the solution is removed and then the device is rinsed with milli-Q water;
4. a solution with the antibody (1 mg/ml) in a phosphate buffer is prepared: for the buffer, it is used 0.1 M of sodium phosphate, 0.3 M of NaCl 0.01% Triton X100 with pH 7.2;
5. the solution with the antibody is placed and kept on the metallic surface for 10/15 hours (overnight exposure);
6. the solution is then removed, the device is rinsed in milli-Q water and dried with compressed air (or N_2 when available).

- *Data analysis*
  Acquired data need to be fitted for the measurements bench behavior. The fitting curve used can be written in the following form:

  $$y(x) = A + Be^{-\frac{(x-C)^2}{D^2}} + Ee^{-\frac{(x-F)^2}{G^2}} \tag{4.5}$$

  which corresponds to two Gaussian functions: B and E are the amplitude value, C and F are the mean value and D and G are the standard deviations. Two Gaussian curves are used because the shape of the Kretschmann peak is quite similar to the shape of a Gaussian function. Those data are then corrected by traslating the curve through the reference value 0.62^o to set a fix setup error (see Chapter 3).
  To perform this data analysis and correction a MATLAB software is developed. It indicates the value of the minimum of reflectance and it plots the desired curves.

4.3 Kretschmann Bench Characterization

As previously stated, all measurement benches have a specific error measurement. This error can be described by analyzing the repeatability of a mesurement: the system should be able to reproduce the same range of values when the bench has the same settings. By knowing the precision of the bench measurement system it is possible to understand the confidence interval.

4.3.1 Intrinsic Error of the Bench

To uderstand the intrinsic error of the measurement bench, two kinds of analyses can be performed:

- the repeatability of the measurement without removing the prism, which can reveal intrinsic errors of the measurement bench.
  For this analysis a bare Ag device (composed by a layer silver and a substrate of polycarbonate) of O.D. of 1500 is measured 20 times, following the *measurement protocol* presented in Section 4.1. The prism with refractive index $n = 1.47$ is used.
  Results are plotted in Figure 4.6. Analysing the results without the fitting curve, no angular shift can be observed for repeated measurements, i.e. susequent measurements without system perturbations. Hence, the bench presents a good repeatability of the measurement.

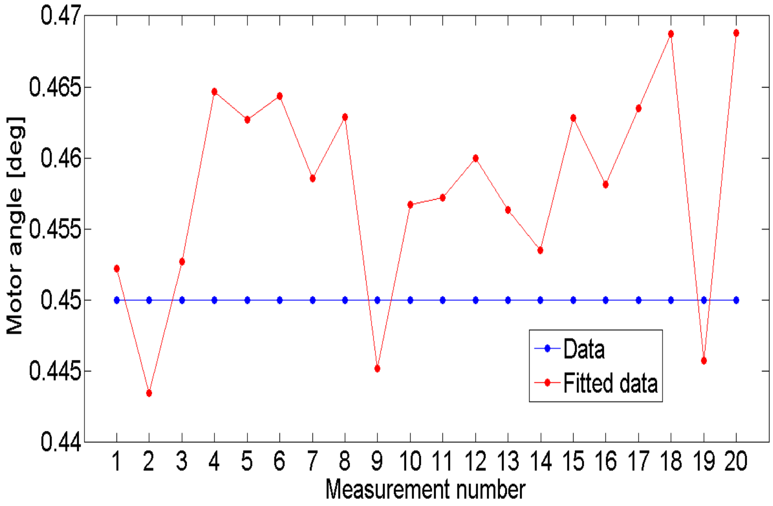

Figure 4.6: SPPs excitation position as a function of the measurement number - analysis with fitting curve (red curve) and without fitting curve (blue curve). Analysis without the unmounting of prism/device

Analysing the results with the fitting curve, we can note a variation that is smaller than the acquisition step, i.e., 0.05^o mainly due to the strong dependence of this analysis from the reflectance value observed by the photodiode. The light acquisition at the photodiode is corrupted by noise, and this noise is reflected into the fitting curve by this variation of the peak position.
After this analysis it is possible to assure a good repeatability of the measurements after the prism/sample coupling with matching oil.

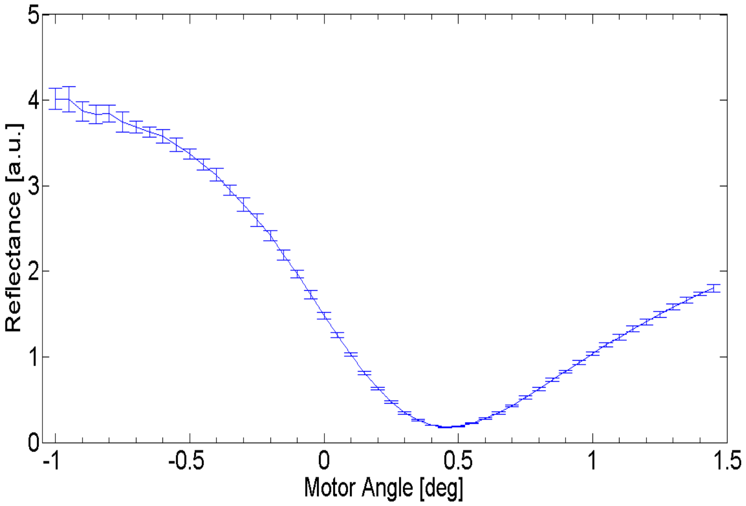

Figure 4.7: Mean and standard deviation of reflectance over 20 measurements for the repeated measurements

- the repeatability with remotion of prism/device, which can reveal errors due to both prism mounting and prism/sample coupling.
  For this analysis a flat bare Ag device of O.D. 1500 is measured following the *measurement protocol* explained in section 1. The prism has a refractive index of $n = 1.47$; the measure is repeated 20 times, unmounting and re-mounting the device from and onto the prism in its socket before each new measurement.

  Experimental data and relative fit are plotted in Figure 4.8: from the analysis it is possible to observe that the error due to the measurement bench corresponds to 0.1^o.
  Concerning the prism/device coupling operation, there could be three sources of error:

  - a little movement of the prism/device in the socket structure, allowing a little change of the initial position. This can be eliminated by better fixing the prism to the socket;
  - the noise measured by the photodiode that is related to intrinsic features of both laser source and photodiodes;
  - the coupling between the prism and the device - the Cargille oil can introduce a coupling error (i.e. some air bubbles can be trapped between the prism and the device).

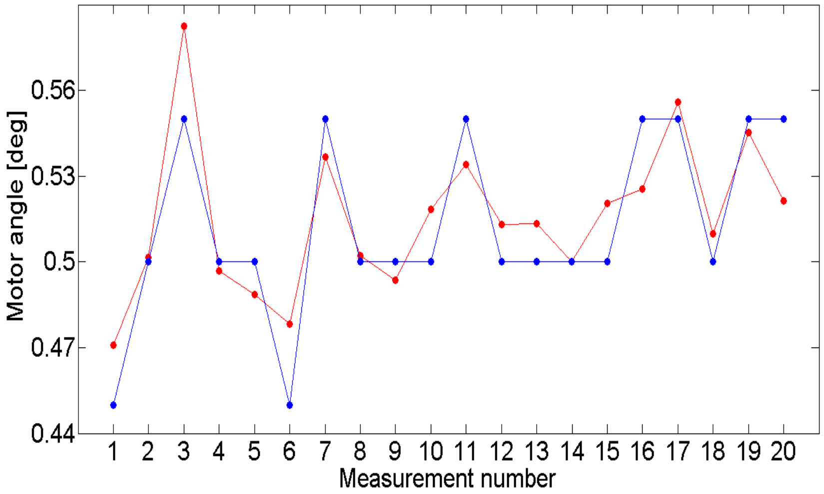

Figure 4.8: SPPs excitation position as a function of the measurement number - analysis with fitting curve (red curve) and without fitting curve (blue curve). Before each measurement the sample has been coupled to the prism.

4.3.2 Delay Time Analysis

As stated in Chapter 3, the data acquisition system operates a step-by-step procedure. At first, the motor supporting the prism/device reaches the desired position; then, after a delay time t_{d_1}, there is the acquisition of 1000 samples. After that, another delay time t_{d_2} is waited before another movement of the motor takes place i.e. the following step acquisition. This procedure is schematized in Figure 4.9.

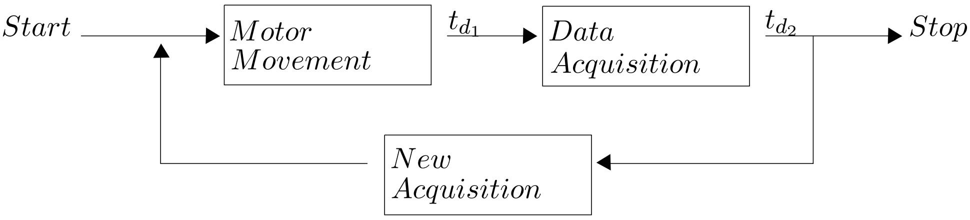

Figure 4.9: Step-by-step acquisition process schematized. Delay time parameters are those values modified in delay time analysis

For all these steps, the entire scanning time could be quite high. In order to be sure that reducing those delays does not compromise the measurement, it is necessary to compare the results obtained using a high delay time with those obtained using a low delay time. If they are reasonably similar, it is possible to use the lowest delay time configuration to improve the acquisition performance.

In this experiment, a flat device of O.D. 1500 is used. Following the *measurement protocol*, the measurement is repeated with the following scheme:

		t_{d_1}				
		$50ms$	$100ms$	$500ms$	$1s$	$2s$
t_{d_2}	$50ms$	5				
	$100ms$		5	5	5	5
	$500ms$		5	5	5	
	$1s$		5	5	5	3
	$2s$		5		3	3

Results are reported in table and depicted in Figure 4.10.

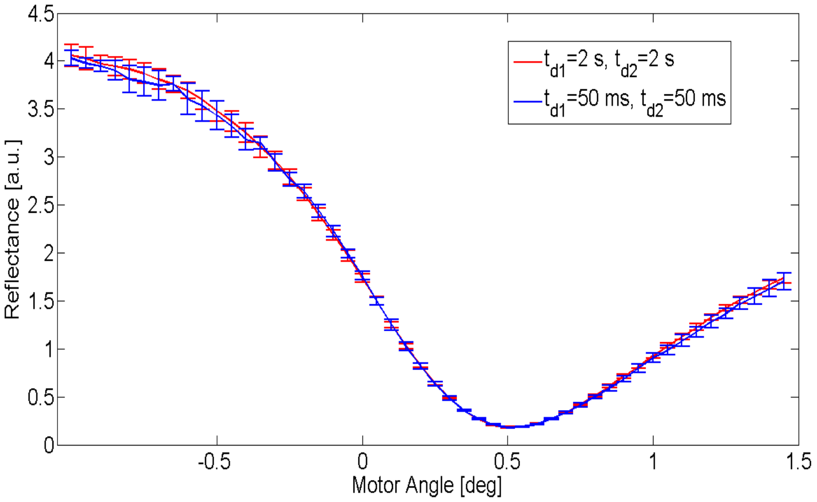

Figure 4.10: Mean value and standard deviation of reflectance as a function of motor angle for the two most different configurations: the red curve represents $t_{d_1} = 50ms$ and $t_{d_2} = 50ms$; the blue curve represents $t_{d_1} = 2s$ and $t_{d_2} = 2s$

Mean SPPs excitation position and standard deviation [deg]						
		t_{d_1}				
		$50ms$	$100ms$	$500ms$	$1s$	$2s$
t_{d_2}	$50ms$	0.5				
	$100ms$		0.5	0.5	0.5	0.5
	$500ms$		0.5	0.5	0.5	
	$1s$		0.5	0.5	0.5	0.5
	$2s$		0.5		0.52 ± 0.03	0.5

As it is possible to see from Figure 4.10 and from the results table, this experiment shows no modification of data varying delay times - hence, it is possible to use the lowest time configuration in order to reduce the acquisition time.

4.4 Device with Grating Structure

As introduced in Chapter 2, grating structure on a substrate of transparent medium can lead to two reasonance peaks. If a grating device is used in prism coupling, there will be two resonance peaks: one due to the metal/air interface, referred as the *Kretschmann peak* which depends on the functionalization of the metallic surface, and one due to the metal/polycarbonate interface, referred as *grating peak* which is almost independent on the functionalization. For this reason, grating devices coupled to prism have a greater potentiality than flat devices: by presenting two peaks instead of one, it is possible to use the *grating peak* as a reference value for precise measures pre and after functionalization and immobilization procedure.

For this experiment, five devices Ag O.D. 2500 are used, each one with a different ϕ angles for the grating structure ($\phi = 0^o$, $\phi = 10^o$, $\phi = 20^o$, $\phi = 30^o$ and $\phi = 40^o$). Each device is then measured as reported in *measurement protocol* with a prism whose refractive index of $n = 1.47$, scanning from -20^o to $+20^o$ with a step of 0.2^o to observe both peaks (Kretschmann, due to the metal/dielectric interface, and grating, due to metal/substrate interface).

Results of the experiment are plotted in Figure 4.11. As it is possible to see from the figure, a change in the ϕ angle corresponds to a change of the position of grating peak, as expected.

Considering that the incident angle of the light on the polycarbonate/metal interface depends on the motor angle (see Figure 4.12) as expressed from the formula

$$\theta_{poly} = \arcsin\left(\frac{n_p \sin\left(\arcsin\left(\frac{n_{air}\sin\theta_{motor}}{n_p}\right) + 45^o\right)}{n_{poly}}\right) \tag{4.6}$$

it is possible to obtain, from measured data, the position peak (in terms of motor angle θ_{motor} and the calculated θ_{poly}) due to grating for each angle ϕ:

ϕ	θ_{motor}	θ_{poly}
0^o	-12.4^o	32.93^o
10^o	-12.4^o	32.93^o
20^o	-11.2^o	33.69^o
30^o	-6.8^o	36.27^o
40^o	-4.4^o	37.69^o

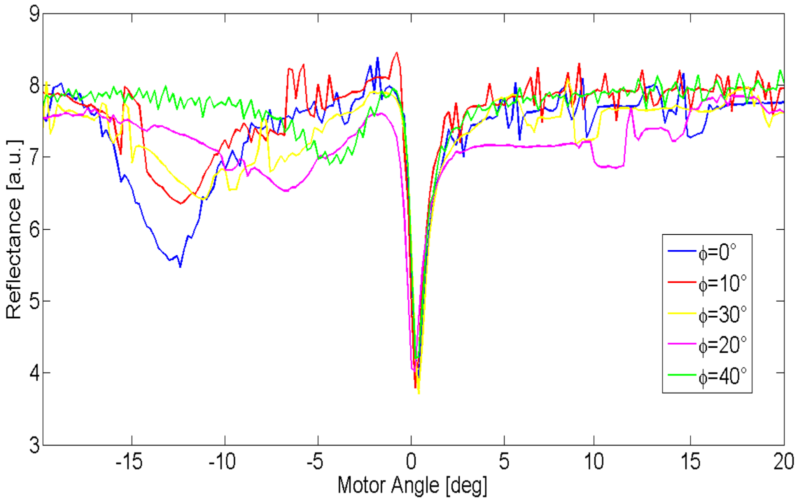

Figure 4.11: Reflectance as a function of motor angle for 5 devices - each one with a different ϕ angle.

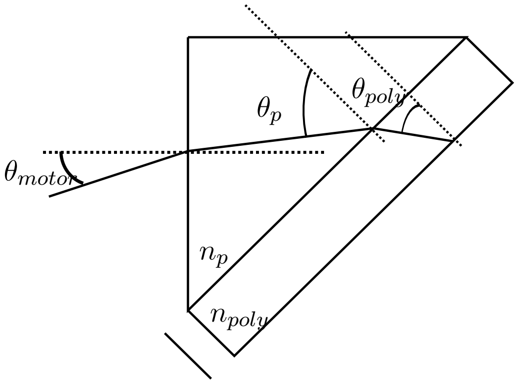

Figure 4.12: Motor angle θ_{motor} and incident angle on polycarbonate/metal surface θ_{poly}

Data are compared in Figure 4.13 with the simulated results of the wavevector model, considering for the simulation the following parameters: $\lambda = 633$ nm, $\Lambda = 740$ nm, $n_{poly} = 1.586$, $n_{metal} = \sqrt{-17 - j0,7}$. From Figure 4.13 it is possible to see that experimental results agree quite well with simulated results.

However, even if the experimental data of the grating peak agree with the theory, each configuration tested is severely corrupted by noise, as it is possible to observe in Figure 4.11. The grating peak, which should work as a reference value because of its almost independence on the dieletric, is not clear and, therefore, it cannot be used as a reference in the peak shift

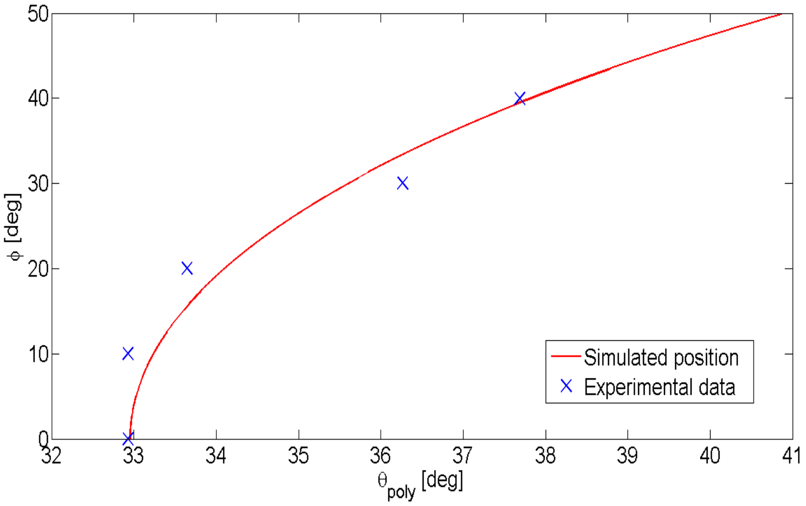

Figure 4.13: Experimental position of the Grating peak (in terms of θ and ϕ). Wavevector model is used for the simulated position.

quantification. Conversely, Krestchsmann peak is well-defined, i.e. the noise does not disturb it.
Hence, from now, for the experimental results of this thesis, flat devices will be the only devices tested.

4.5 Bare Devices Characterization of Flat Ag O.D. 1500

The starting point for the development of the Biological aspect of a SPR biosensor is the characterization of a bare (or *fresh*) Ag flat device: the device, composed only by a layer of metal (in this case silver) and a supporting substrate of polycarbonate, needs to be described in terms of SPPs excitation position. Two different kind of analyses can be performed:

- analysis of **different devices**.
  When considering different devices with the same nominal optical density the real variation from this theoretical value must be taken into account.
  For this experiment, 21 Ag flat devices are measured, following the *measurement protocol* in Chapter 4. The prism refractive index is $n = 1.47$.

  Results are reported in the following table:

SPPs excitation position [deg] - fitted data	
Mean value θ_{motor}	0.570
Standard deviation σ	0.085
Range $\theta_{max} - \theta_{min}$	0.294

This analysis results in a quite high variability of the resonance peak position, variability which can be an expression of the lack of uniformity of the silver layer. Hence, a precise standard value for the resonance position is difficult to be enstablished. The range of values for the resonance peak position is approximately 0.3^o.

- analysis of different spots in the **same device**.
  When considering a single device, it is possible to notice a lack of uniformity of the metal thickness: changing the area hit by the laser there could be a change in SPPs excitation position. To investigate it, multiple spots on the same devices are measured, following the reference scheme of Figure 4.14

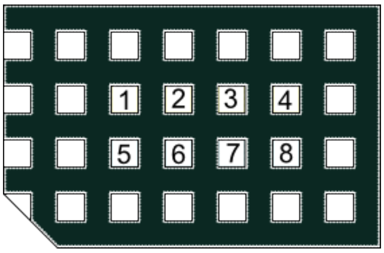

Figure 4.14: Measured spots on the device surface

The methodology used is the *measurement protocol* explained in Chapter 4. To make the laser light hit the right spot it is necessary to move vertically the base supporting the prism until the ray hits the correct raw. Then the device is moved orizontally on the prism surface until the desired spot is reached. The prism used has a refractive index of $n = 1.51$. 3 devices are measured on those spots, for 24 total measures. Fitted results are reported in the following table:

SPPs excitation position [deg] - fitted data			
	Device 1	Device 2	Device 3
Mean value θ_{motor}	-2.839	-2.858	-2.78
Standard deviation σ	0.034	0.041	0.051
Range $\theta_{max} - \theta_{min}$	0.121	0.140	0.125

We can observe again a quite high variability of SPPs excitation position - hence, in the same device the layer of metal does not seem to have a uniform thickness.

Because of this quite high variability in the metal deposition, in order to reach the highest possible degree of precision, measures will be collected before and after the functionalization of the surface on the same position. This methodology reduces the error due to this variability of metal thickness. An example curve of reflectance for a device in *fresh* condition (when $n_{prism} = 1.51$) is depicted in Figure 4.15. It can be compared with the simulated behaviour (depicted in Figure 4.16) obtained using the simulation software described in Chapter 3. In it, the following parameters are considered:

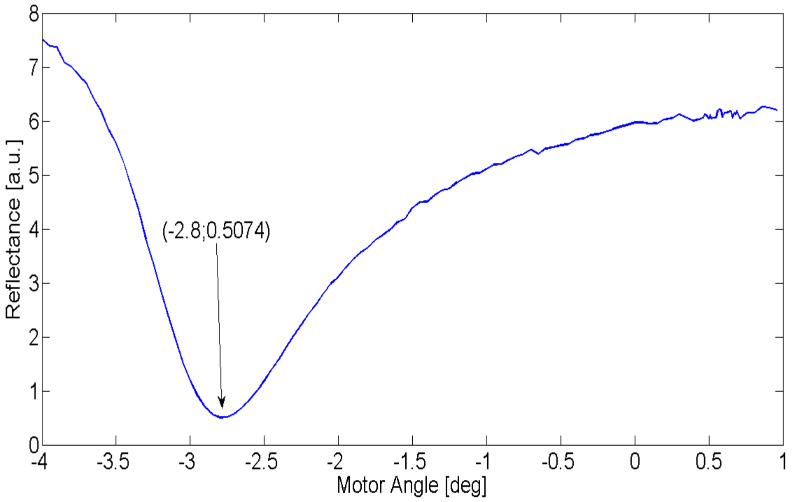

Figure 4.15: Example of reflectance curve for the *fresh* condition

- $\lambda = 633$ nm for the laser wavelength;
- layer 1: glass prism with $n_p = 1.51$;
- layer 2: polycarbonate with refractive index $n_{poly} = 1.586$ and thickness $d_{poly} = 600\ \mu m$;
- layer 3: silver with refractive index $n_{metal} = \sqrt{-17 - j0.7}$ and thickness $d = 40$ nm (which corresponds to an optical density of 1500);
- air layer with $n = 1$.

As it is possible to see from the comparison of these two figures, the experimental results well suit the simulated one.

4.6 PEG 1 mM Functionalization Test

In this experiment, Ag flat O.D. 1500 devices are functionalized with PEG 3400 Dalton 1mM. The main aim is to test the adsorption of PEG molecule

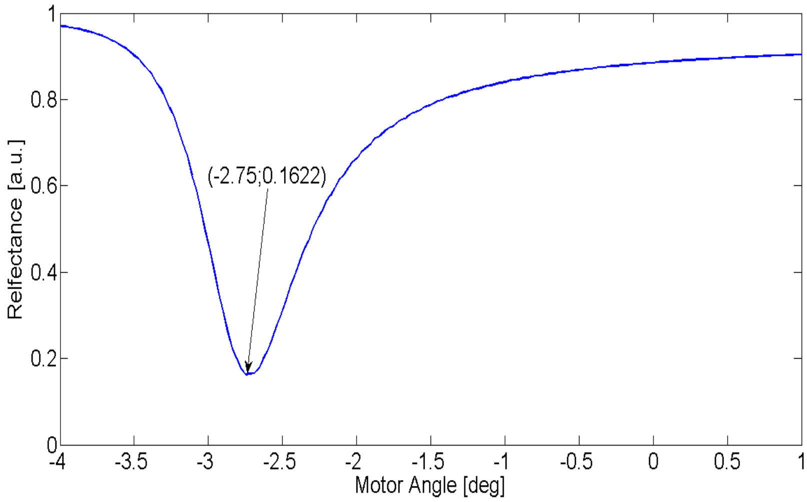

Figure 4.16: Simulated results for *fresh* condition

onto the silver surface and to compare experimental with simulated results. Devices are cleaned following the *cleaning protocol*; then they are mesured in 8 spots for each of them following the *measurement protocol*. Devices are functionalized following the *functionalization protocol* with the scheme of Figure 4.17; then they are measured again in the same spots measured before the overnight exposure. It should be noticed that some spots are not

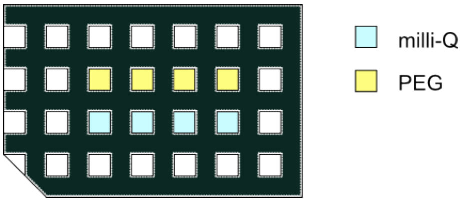

Figure 4.17: Mask configuration used for PEG test.

functionalized but are kept fresh through the contact with milli-Q water: it is necessary to observe if the night exposure has the side effect of modyfing the SPPs excitation position.

The reference values in this analysis are the fresh and milli-Q exposure excitation positions: we will considered the angular shift as the substraction of two different SPPs excitation position due to different functionalization stage. Some experiments are performed, leading to the following results:

SPPs excitation position [deg] - fitted data		
Experiment	1	2
Total spots tested	16	16
Fresh position	-2.80 ± 0.06	-2.84 ± 0.04
Milli-Q exposure	-2.59 ± 0.05	-2.71 ± 0.05
PEG 1 mM	-1.59 ± 0.13	-2.23 ± 0.12
Shift respect to average [deg]		
Shift milli-Q/fresh	0.20 ± 0.05	0.12 ± 0.04
Shift PEG/fresh	1.22 ± 0.10	0.69 ± 0.12
Shift PEG/milli-Q	1.00 ± 0.13	0.48 ± 0.12

SPPs excitation position [deg] - fitted data		
Experiment	3	4
Total spots tested	16	16
Fresh Position	-2.85 ± 0.05	-2.81 ± 0.04
Milli-Q exposure	-2.77 ± 0.08	$-2,63 \pm 0.06$
PEG 1 mM	-2.14 ± 0.19	-1.52 ± 0.19
Shift respect to average [deg]		
Shift milli-Q/fresh	0.07 ± 0.08	0.16 ± 0.03
Shift PEG/fresh	0.70 ± 0.20	1.31 ± 0.21
Shift PEG/milli-Q	0.63 ± 0.19	1.11 ± 0.19

As it is possible to observe in the table, in each experiment a good repeatability can be achieved: the standard deviation is reasonably low. However, different experiments still suffer quite low repeatability, probably caused by small difference between materials involved, such as PEG powder or milli-Q water. Furthermore, PEG 3400 Dalton is a molecule with a very long chain of OCH_2CH_2; hence, the arrangement on the metal layer could not be fixed in different experiments.

Experimental results can be compared with the simulated ones obtained using MATLAB software. The parameters considered are:

- $\lambda = 633$ nm for the laser wavelength;
- layer 1: glass prism with $n_p = 1.51$;
- layer 2: polycarbonate with refractive index $n_{poly} = 1.586$ and thickness $d_{poly} = 600\ \mu m$;
- layer 3: silver with refractive index $n_{metal} = \sqrt{-17 - j0.7}$ and thickness $d = 40$ nm (which corresponds to an optical density of 1500);
- layer 4: PEG with a refractive index $n = 1.5$ and thickness $d = 5$ nm;
- layer 5: air with $n = 1$.

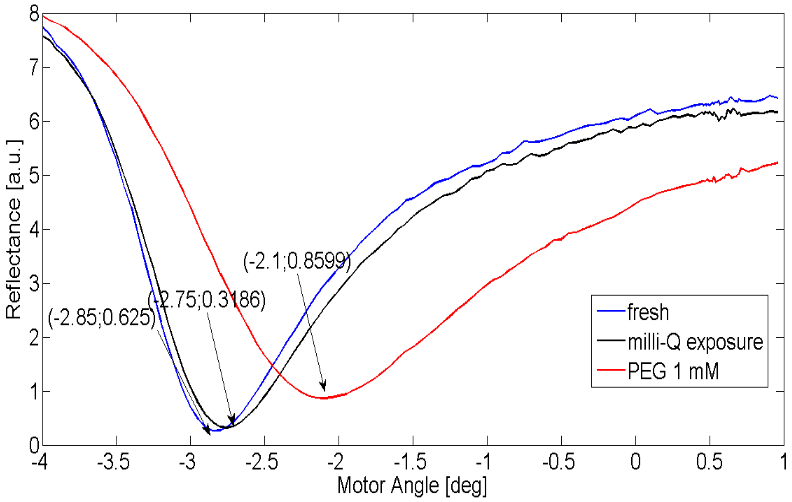

Figure 4.18: Mean value of reflectance for experiment 2. Fresh condition in blue (16 spots), milli-Q exposure in black (8 spots), PEG 3400 Dalton 1mM in red (8 spots).

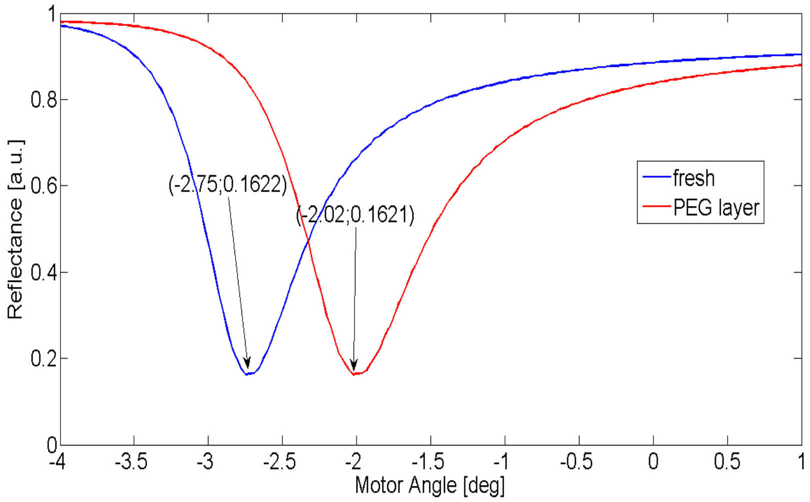

Figure 4.19: Simulated results for *fresh* and PEG layer

For this value of PEG 3400 concentration, because of this high variability of results, it is possible to calculate a range of sensitivity of the measurement bench.

For the calculation of sensitivity, it is assumed that the adsorbate layer consists in a uniform layer of thickness d and refractive index of value n_a grown onto the metal surface. Above this adsorbate layer, we consider a bulk liquid solution whose refractive index is n_s.

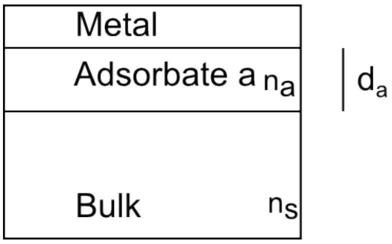

Figure 4.20: Structure considered for the calculation of n_{eff}

Hence, the sensitivity we calculate is

$$S = \frac{\Delta\theta}{\Delta n_{eff}}, \tag{4.7}$$

where n_{eff} is the effective refractive index of the bilayer adsorbate/bulk whose value is given by [47]

$$n_{eff} = n_s + (n_a - n_s)\left[1 - e^{-\frac{2d_a}{\hat{z}}}\right]. \tag{4.8}$$

In this equation, $\hat{z}$ is the characteristic decay length in the dielectric medium (2.49) and d is the thickness of the adsorbate layer.
Considering $n_s = 1$ (air), $n_a = 1.5$ (the PEG layer assumed in the simulation) and $n_{metal} = \sqrt{-17 - 0.7j}$

$$\hat{z} = \frac{633nm}{2\pi}\sqrt{\frac{17 + 2.25}{2.25^2}} = 196nm \tag{4.9}$$

and

$$n_{eff} = 1 + 0.5\left[1 - e^{-0.05102}\right] = 1.025 \tag{4.10}$$

from which it is possible to get the following table for sensitivity:

	Sensitivity $\frac{[deg]}{[RIU]}$			
Experiment	1	2	3	4
$\frac{\Delta\theta}{\Delta n_{eff}}$	40	19.2	25.6	44.2

Therefore, the sensitivity range goes approximately from 19.2 to 44.2 $\frac{[deg]}{[RIU]}$.

4.7 PEG Concentration Test

Various concentration of PEG 3400 Dalton can be tested: this experiment can reveal which is the lowest detectable concentration of PEG and how the different concentration influeces the angular shift.
In this experiment 2 devices are used, for 16 total spots measured. The concentration considered are: PEG 3400 Da 0.1 mM, PEG 3400 Da 0.5 mM and PEG 3400 Da 1 mM.
The devices are at first cleaned following the *cleaning protocol*, then they are measured in their *fresh* condition. They are functionalized with the three solutions created following the *diluition protocol*; after the overnight exposure the devices are re-measured again.
In this experiment, a prism of refractive index of $n = 1.51$ is used. The following table shows the results:

Mean and standard deviation for SPPs excitation [deg]	
Fresh position	-2.75 ± 0.07
Milli-Q exposure	-2.65 ± 0.05
PEG 0.1 mM	-2.56 ± 0.06
PEG 0.5 mM	-2.235 ± 0.07
PEG 1 mM	-2.01 ± 0.16
Mean and standard deviation for shift respect to average [deg]	
Shift milli-Q/fresh	0.04 ± 0.04
Shift 0.1 mM/fresh	0.19 ± 0.04
Shift 0.1 mM/milli-Q	0.08 ± 0.06
Shift 0.5 mM/fresh	0.55 ± 0.03
Shift 0.5 mM/milli-Q	0.41 ± 0.07
Shift 1 mM/fresh	0.76 ± 0.12
Shift 1 mM/milli-Q	0.64 ± 0.16

The mean value curves for each concentration are plotted in Figure 4.21. From the experimental data obtained, it is possible to infer that the lowest concentration detected is 0.1 mM.

4.8 PEG Functionalization and Antibodies Immobilization Test

After the creation of a PEG SAM onto the metal surface, the antibodies immobilization has to be tested. However, the entire process requires two overnight exposures, hence more manipulation of the devices. To avoid the undesiderable contact between the coupling Cargille oil and the metal surface, we do not measure the fresh condition before the functionalization but we choose to use the milli-Q exposure as the reference value for the shift

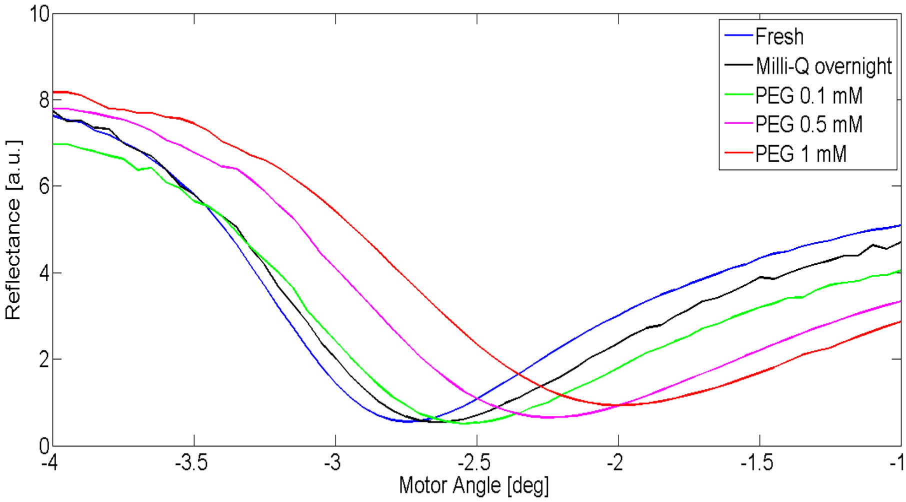

Figure 4.21: Mean value curves for *fresh* condition, milli-Q exposure, PEG 3400 Dalton 0.1 mM, 0.5 mM, 1 mM.

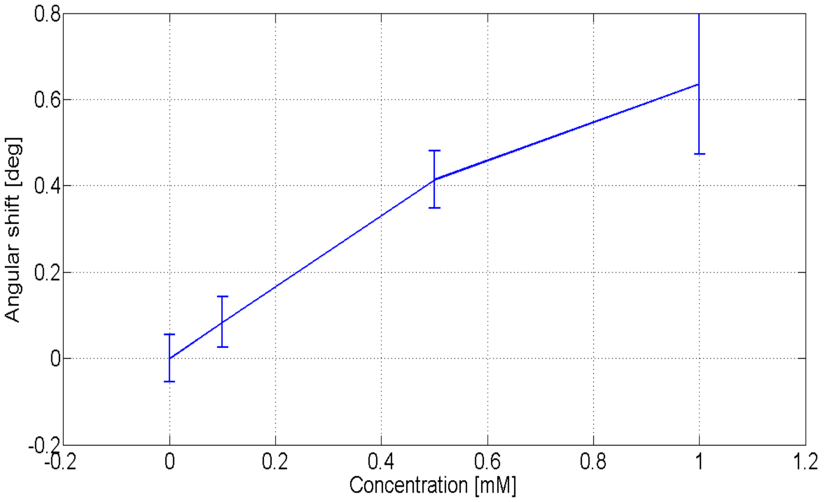

Figure 4.22: Mean values and standard deviations for Shift PEG/milli-Q as a function of PEG concentration.

calculation.
The procedure is organized as follows:

- devices are cleaned following the *cleaning protocol*;
- devices are functionalized following the *functionalization protocol*;

- antobodies are immobilized onto the surface following the *immobilization protocol*;
- devices are measured following the *measurement protocol.*

3 devices are tested, for a total of 24 spots measured (6 of milli-Q, 9 with antibodies immobilized, 9 with PEG 3400 1 mM).

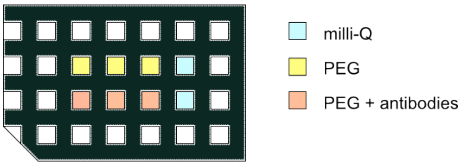

Figure 4.23: Mask configuration used for PEG and antibodies immobilization test.

Results are reported in the following table:

Mean and standard deviation for SPPs excitation [deg]			
Device	1	2	3
Milli-Q exposure	-2.68 ± 0.04	$-2,71 \pm 0.02$	-2.45 ± 0.01
PEG 1 mM	-1.71 ± 0.12	-1.9 ± 0.19	-1.75 ± 0.06
PEG 1 mM + antibodies	-1.35 ± 0.11	-1.43 ± 0.25	-1.56 ± 0.22
Mean and standard deviation for shift respect to average [deg]			
Shift 1 mM/milli-Q	0.97 ± 0.12	0.80 ± 0.19	0.70 ± 0.06
Shift PEG + anti/milli-Q	1.33 ± 0.11	1.28 ± 0.25	0.89 ± 0.22
Shift PEG + anti/PEG	0.37 ± 0.11	0.48 ± 0.25	0.19 ± 0.22

The measurement bench can recognize the antibodies immobilized onto the surface, distinguishing them from the only PEG layer. However, as in the PEG case, a high variability of the measures is observed.
A simulation can be performed, considering the following parameters:

- $\lambda = 633$ nm;
- layer 1: glass prism with $n_p = 1.51$;
- layer 2: polycarbonate with refractive index $n_{poly} = 1.586$ and thickness $d_{poly} = 600\ \mu m$;
- layer 3: silver with refractive index $n_{metal} = \sqrt{-17 - j0.7}$ and thickness $d = 40$ nm (which corresponds to an optical density of 1500);
- layer 4: PEG with a refractive index $n = 1.5$ and thickness $d = 5$ nm;
- layer 5: antibodies immobilized onto PEG with a refractive index $n = 1.45$ and thickness $d = 5$ nm;

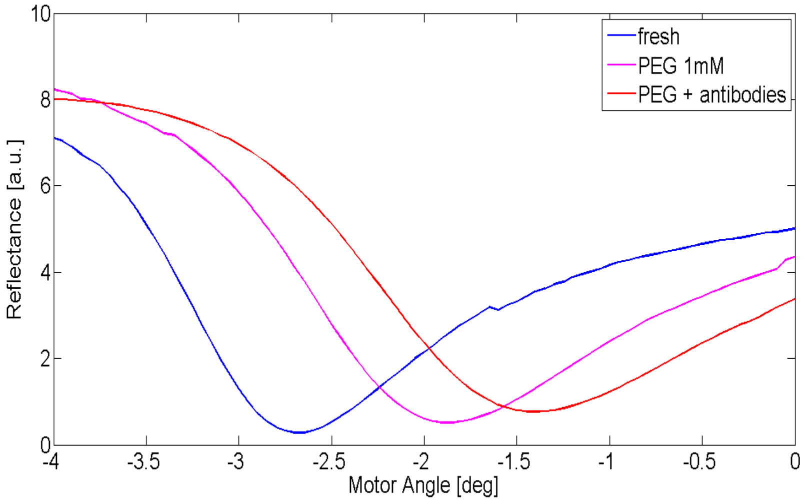

Figure 4.24: Mean value curves for milli-Q exposure, PEG 3400 Da 1 mM, and PEG 3400 Da + antibodies of the second device.

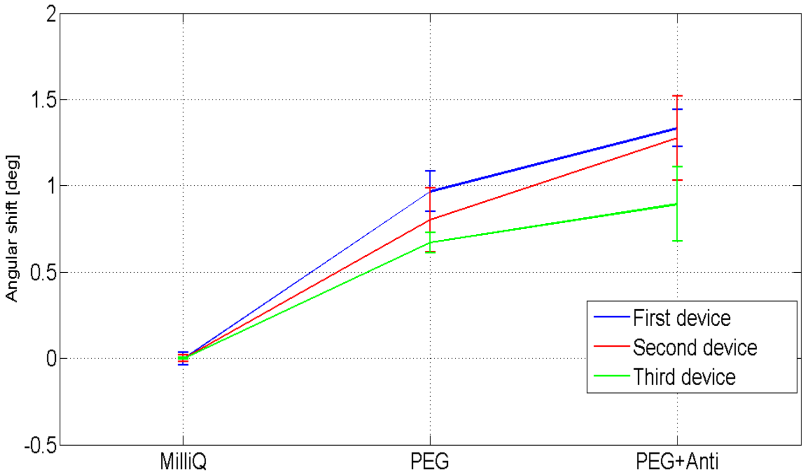

Figure 4.25: Mean value and standard deviation of shift respect to milli-Q exposure. Plotted results of three devices.

- layer 5: air with $n = 1$.

This configuration leads to results depicted in Figure 4.26.

As in the PEG case, it is possible to calculate the sensitivity of the measurement bench. In this case, to calculate the effective refractive index,

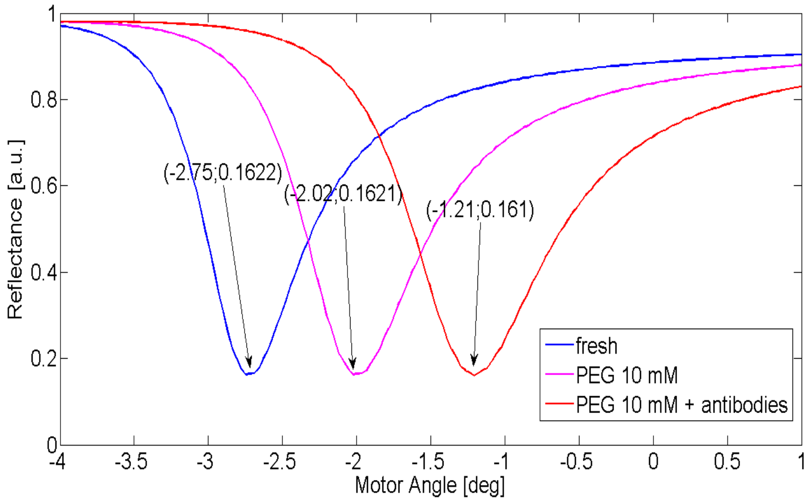

Figure 4.26: Simulated results for fresh, PEG 1 mM and PEG 1 mM + antibodies.

we need to consider three layers of adsorbates [47], leading to the following

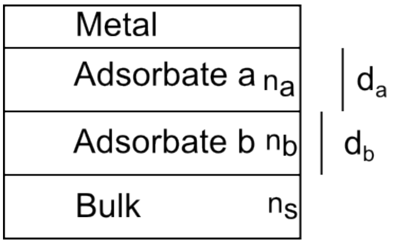

Figure 4.27: Structure considered for the calculation of n_{eff}

relation:

$$n_{eff} = n_b\left[1-e^{\frac{-2d_b}{\hat{z}}}\right] + n_a\left[e^{\frac{-2d_b}{\hat{z}}} - e^{\frac{-2(d_a+d_b)}{\hat{z}}}\right] + n_s e^{\frac{-2(d_a+d_b)}{\hat{z}}} \tag{4.11}$$

Hence, using those parameters considered for the simulation, we get the value

$$n_{eff} = 1.5\left[1-e^{-0.051}\right] + 1.45\left[e^{-0.051} - e^{-0.102}\right] + e^{-0.102} = 1.045 \tag{4.12}$$

from which it is possible to calculate the sensitivity parameter for the antibodies layer:

$$S = \frac{\Delta\theta}{\Delta n_{eff}} = \frac{\theta_{PEG+anti} - \theta_{PEG}}{n_{eff_{PEG+anti}} - n_{eff_{PEG}}} \tag{4.13}$$

	Sensitivity $\frac{[deg]}{[RIU]}$		
Device	1	2	3
$\frac{\Delta\theta}{\Delta n_{eff}}$	18.5	24	9.5

As in the PEG case, because of the variability of results obtained, we get a range of values for sensitivity. It is comparable with that one calculated with the PEG layer only.

Chapter 5

Conclusions

In this Thesis we used a Kretschmann measurement bench improved with a photodiode array for position identification to develop a precise SPR biosensor. This photodiodes array detects the laser beam reflected by the prism face, in order to implement a control of the prism positioning. Thanks to this upgrade the repeatability of the optoelectronic measurement system can be improved, making the bench suitable for the precise measures required for bacteria recognition.

The experimental research performed confirmed that the Kretschmann measurement bench can be used to create a SPR biosensor for PEG molecules and rat polyclonal antibodies anti-Escherischia Coli layer recognition. Employing 40 nm thick silver metal devices provided by Next Step Engineering (University of Padova spin-off), it has been shown that the SPR sensor can distinguish each of the layers considered from the previous condition of the device:

- the PEG layer can be discerned from the bare condition, identifying a shift of about $0.6/1^o$;
- the antibodies layer can be discerned from the PEG layer, identifying a shift of about 0.4^o;

as predicted by the simulation software implemented.

However, the target molecule has not been tested yet; further scientific experiments involving the target molecule need to be performed to experimentally prove the bacteria detection.

Ringraziamenti
Si ringrazia per la collaborazione lo staff di *Veneto Nanotech* e di *Next Step Engineering.*

Bibliography

[1] R. W. Wood (1902), *On a remarkable case of uneven distribution of light in a diffraction grating spectrum*, Proceedings of the Physical Society 18:269-275

[2] U. Fano (1941), *The Theory of Anomalous Diffraction Gratings and of Quasi-Stationary Waves on Metallic Surfaces (Sommerfeld's Waves)*, JOSA, Vol. 31, Issue 3, pp 213-222, Journal of the Optical Society of America

[3] M. Midrio (2003), *Campi Elettromagnetici*, S.G.E. 2003

[4] S. A. Maier (2007), *Plasmonic - Fundamentals and Application*, Springer

[5] N. A. Riza (2013), *Photonic Signals and Systems: An Introduction*, Mc Graw Hill Education

[6] J. R. Sambles, G. W. Bradbery and F. Yang (1991), *Optical Excitation of Surface Plasmons: an Introduction*, Contemporary Phsysics volume 32 number 3 173-183

[7] J. D. Jackson (1999), *Classical Electrodynamics*, Wiley

[8] F. A. Jenkins, H. E. White (1981), *Fundamentals of Optics*, Mc Graw Hill

[9] H. Raether (1986), *Surface Plasmons on Smooth and Rough Surfaces and on Gratings*, Springer-Verlag

[10] J. Homola (2006), *Surface Plasmon Resonance Based Sensors*, Springer-Verlag

[11] E. Kretschmann (1971), *Die Bestimmung optischer Konstanten von Metallen durch Anregung von Oberflächensplasmaschwingungen*, Zeitschrift für Physik

[12] J. Bösenberg (1971), *Photoelectrons from optically excited nonradiative surface plasma oscillation*, Physics Letters A37 Issue5 pages 439-440

[13] R. A. Watts, J. B. Harris, A. P. Hibbins, T. W. Preist, J. R. Sambles (1996), *Optical excitation of surface plasmon polaritons on 90 and 60 bi-gratings*, Journal of modern optics vol 43 no. 7 1351-1360

[14] A. V. Zayats, I. I. Smolyaninov, A. A. Maradudin (2005), *Nano-optics of surface plasmon polaritons*, Physics Reports 408 131-314

[15] S. J. Elston, G. P. Bryan-Brown (1991), *Polarization Conversion from Diffraction Gratings*, Phys. Rev. B 44 6393-6400

[16] A. Karabchevsky, O. Krasnykov, M. Auslender, B. Hadad, A. Goldner, I. Abdulhalim (2009), *Theoretical and Experimental Investigation of Enhanced Transmission Through Periodic Metal Nanoslits for Sensing in Water Environment*, Plasmonics volume 4 issue 4 281-292

[17] I. Abdulhalim (2012), *Patent: Optical sensor with enhanced sensitivity* WO 2012/111001 A2

[18] J. G. Gordon II, S. Ernst (1980), *Surface Plasmons as a Probe of the Electrochemical Interface*, vol. 101 issues 1-3 pp 499-506

[19] C. Nylander, B. Liedberg, T. Lind (1982-1983), *Gas Detexction by Means of Surface Plasmon Resonance*, Sensors and Actuators vol.3 79-88

[20] C. Narduzzi (2011), *Dispense di Misure Elettroniche*, 1 Parte, Edizioni Libreria Progetto Padova

[21] E. D. Palik (1998), *Handbook of Optical Constants of Solids*, Academic Press

[22] J. Homola, I. Koudela, S. S. Yee (1999), *Surface Plasmon Resonance Sensors Based on Diffraction Gratings and Prism Couplers: Sensitivity Comparisons*. Sensors and Actuators 16-24

[23] J. Yuan, R. Oliver, J. Li, J. Lee, M. Aguilar, Y. Wu (2007), *Sensitivity Enhancement of SPR Assy of Progesterone Based on Mixed Self-Assembled Monolayers Using Nanogold Particles*, Biosensors and Bioelectronics 23 1 144-148

[24] F. Romanato, K. H. Lee, H. K. Kang, G. Ruffato, C. C. Wong (2009), *Sensitivity Enhancement in Grating Coupled Surface Plasmon Resonance by Azimuthal Control*, Optics Express 17 14 12145-12154

[25] M. Piliarik, J. Homola (2009), *Surface Plasmon Resonance (SPR) Sensors: Approaching Their Limits?*, Optics Express 17-19 2009

[26] V. Thomsen, D. Schatzlein, D. Mercuro (2003), *Limits of Detection in Spectroscopy*, Spectroscopy 18(12) 112-114

[27] J. C. Love, L. A. Estroff, J. K. Kribel, R. G. Nuzzo and G. M. Whitesides (2005), *Self-Assembled Monolayers of Thiolates on Metals as a Form of Nanotechnology*, Chem. Rev. 105, 1103-1169

[28] R. G. Nuzzo, D. L. Allara (1983), *Absorption of Bifunctional Organic Disulfides on Gold Surfaces*, Journal of Chemical Society 105, 4481-4483

[29] Acs Symposium Series (1997), *Poly(ethylene glycol) - Chemistry and Biological Applications*, American Chemical Society

[30] T. W. Schneider, D. A. Buttry (1993), *Electrochemical quartz crystal microbalance studies of adsorption and desorption of self-assembred monolayers of alkyl thiols on gold*, Journal of American Chemical Society, 115(26) 12391-12397

[31] M. Cerruti, S. Fissolo, C. Carraro, C. Ricciardi, A. Majumdar, R. Maboudian (2008), *Poly(ethylene glycol) Monolayer Formation and Stability on Gold and Silicon Nitride Substrates*, Langmuir 24 10646-10653

[32] M. J. Roberts, M. D. Bentley, J. M. Harris (2002), *Chemistry for Peptide and Protein PEGylation*, Advanced Drug Delivery Reviews, volume 54 issue 459-476

[33] S. S. Banerjee, N. Aher, R. Patil, J. Khandare (2012), *Poly(ethylene glycol)-Prodrug Conjugates: Concept, Design and Applications*, Journal of Drug Delivery article ID 103973

[34] P. G. Basso, F. Bertoncello, T. Biasi, L. Cenci, A. D'Amato, S. Ferrarini, D. Foá, C. Gemo, G. Giaretta, G. Morandin, M. Poli, S. Screamin, G. Pozza, R. Pozzato, A. Vanzo, M. Visoná (2006), *Corso di Formazione per Addetti alla Manipolazione di Alimenti*, a cura dell'Unitá locale socio-sanitaria n.6 Vicenza, Centro Stampa Gennaio

[35] F. Baldacchini, B. M. Borrini, I. Dodi, F. Faccini, A. C. Finarelli, M. Fridel, C. Gualanduzzi, L. L. Piccolomini, A. Mattivi, M. Rosi, G. Squintani, M. Tamba, L. Vicinelli (2011), *Epidemiologia delle Malattie Trasmesse da Alimenti in Emilia-Romagna, Aggiornamento al 2011*, consulted in March 2014 at the website http://www.saluter.it/search?Subject:list=Malattie%20trasmesse%20 da%20alimenti&path=/saluter/documentazione

[36] V. Koubová, E. Brynda, L. Karasová, J. Skvor, J. Dostálek, P. Tobiska, J. Rosicky (2001), *Detection of Foodborne Pathogens Using Surface Plasmon Resonance Biosensors*, Sensors and Actuators B: Chemical volume 74 Issues 1-3 100-105

[37] S. D. Mazumdar, M. Hartmann, P. Kämpfer, M. Keusgen (2007), *Rapit Method for Detection of Salmonella in Milk by Surface Plasmon Resonance*, Biosensors and Bioelectronics 22, 2040-2046

[38] webreference: *http : //www.arpa.emr.it/cms3/documenti/_cerca_doc/mare/progetto_mare/biotossine.htm*

[39] Q. Yu, S. Chen, A. D. Taylor, J. Homola, B. Hock, S. Jiang (2005), *Detection of Low-Molecular-Weight Domoic Acid Using Surface Plasmon Resonance Sensor*, Sensors and Actuators B: Chemical volume 107 Issue 1 193-201

[40] D. Nedelkov, A. Rasooly, R. W. Nelson (2000), *Multitoxin Biosensor-Mass Spectrometry Analysis: a New Approach for Rapid, Real-Time, Sensistive Analysis of Staphylococcal Toxins in Food*, International Journal of Food Microbiology volume 60 issue 1 1-13

[41] W. Tsai, I. Li (2009), *SPR-based Immunosensor for Determining Staphylococcal enterotoxin A*, volume 136 issue 1 8-12

[42] H. V. Hsieh, B. Stewart, P. Hauer, P. Haaland, R. Campbell (1998), *Measurement of Clostridium Perfringens β-Toxing Production by Surface Plasmon Resonance Immunoassay*, Volume 16, Issues 9-10, 997-1003

[43] J. Ladd, A. D. Taylor, J. Homola, S. Jiang (2008), *Detection of Botulinum Neurotoxins in Buffer and Honey Using a Surface Plasmon Resonance (SPR) Sensor*, Sensors and Actuators B: Chemical volume 130 issue 1 129-134

[44] D. Wei, O. A. Oyarzabal, T. Huang, S. Balasubramanian, S. Sista, A. L. Simonian (2007), *Development of a Surface Plasmon Resonance Biosensor fo the Identification of Campylobacter Jejuni*, Journal of Microbiological Methods, volume 69, issue 1 78-85

[45] P. Qi, Y. Li and J. Zhong (2012), *Optimized angle scanning method for array sample detection in surface plasmon resonance biosensor*, Journal of the Optical Society of America

[46] T. E. Furtak, M. V. Klein, *Optics*, Wiley 1986

[47] L. S. Jung, C. T. Campbell, T. M. Chinowsky, M. N. Mar, S. S. Yee (1998), *Quantitative Interpretation of the Response of Surface Plasmon Resonance Sensors to Adsorbed Films*, Langmuir 14 5636-5648